POLITECNICO DI TORINO

POLITECNICO DI TORINO

Master Degree course in Nanotechnologies for ICT

Master Degree Thesis

Analysis and Design of Integrated Mid-Infrared Optical Phased Arrays

Supervisors
Prof. Paolo Bardella
Ing. Lorenzo Tunesi

Candidate
Vito Gliubizzi

Academic Year 2025-2026

Acknowledgements

I would like to thank my family for their constant support throughout these years. Their encouragement and trust have always given me the motivation to move forward, even during the most challenging moments of my studies.

I am especially grateful to my parents, who have always believed in me and supported every step of my academic path. Their patience, their advice, and their continuous encouragement have been essential in helping me reach this important milestone.

More than anything, I am thankful for the values they have taught me and for the example they have always set. Their presence and support have guided me throughout this journey, and this achievement is as much theirs as it is mine.

Abstract

Optical phased arrays (OPAs) represent a promising solution for solid-state beam steering in applications such as LiDAR and optical sensing. In particular, the mid-infrared spectral region is of growing interest due to the presence of strong molecular absorption lines, which makes this wavelength range highly relevant for environmental monitoring and chemical detection.

This thesis investigates the design and numerical analysis of an integrated optical phased array operating between 4 µm and 8 µm on a germanium-on-silicon photonic platform. The work focuses on the design and optimization of the main building blocks required for the implementation of an integrated OPA, including the waveguide platform, the optical power distribution network, the thermo-optic phase shifters, and the emitting array responsible for generating the far-field radiation pattern.

A realistic waveguide model is first developed by incorporating propagation losses reported in the literature into the simulation environment. Based on this model, the geometry of the Ge-on-Si strip waveguide is optimized and suitable routing solutions are identified. The optical power distribution stage is then designed through a comparison between Y-splitters and multimode interference couplers, leading to the implementation of a cascaded MMI architecture capable of feeding a sixteen-element emitter array.

Thermo-optic phase shifters are employed to control the phase of the optical signals in each branch of the array. The thermal response of the structure is analyzed, and the heater geometry is optimized in order to achieve the required phase shift. Finally, the radiation characteristics of the emitter array are investigated and the resulting far-field patterns are evaluated through numerical simulations. Besides beam steering capabilities, the analysis also highlights the possibility of generating more complex radiation patterns by applying different phase configurations to the emitters, suggesting potential applications in structured illumination and computational imaging systems.

The obtained results demonstrate the feasibility of implementing integrated beam steering in the mid-infrared using a germanium-on-silicon platform and provide useful guidelines for the design of compact optical phased array systems.

Contents

1 Introduction 5
- 1.1 Motivation and application context . . . 5
- 1.2 Optical Phased Arrays: operating principle . . . 7
- 1.3 OPA Architectures and Their Impact on the Far-Field Response . . . 8
- 1.4 Physical and Technological Limitations of Mid-Infrared OPAs . . . 11
- 1.5 Simulation Tools and Numerical Methods . . . 12
  - 1.5.1 BeamPROP . . . 13
  - 1.5.2 FullWAVE . . . 13
  - 1.5.3 FemSIM . . . 14
- 1.6 Scope and structure of the thesis . . . 17

2 Waveguide Design for Mid-Infrared Optical Phased Arrays 19
- 2.1 Germanium-on-Silicon Material Platform . . . 20
- 2.2 Optical Properties of Germanium in the Mid-Infrared . . . 20
- 2.3 Numerical Modeling in RSoft . . . 21
- 2.4 Waveguide Geometry Definition . . . 24
- 2.5 Curved Waveguides and Bending Constraints . . . 25
  - 2.5.1 Circular Arc . . . 25
  - 2.5.2 S-Bend Configurations . . . 27
- 2.6 Final Waveguide Geometry . . . 27

3 Optical Power Splitting Network 31
- 3.1 Role of the Power Splitting Stage in Optical Phased Arrays . . . 31
- 3.2 Y-Branch Splitter: Design and Performance at 6 µm . . . 32
- 3.3 MMI 1x2 Splitter: Design and Performance at 6 µm . . . 33
- 3.4 Broadband Analysis in the 4-8 µm Range and Device Selection . . . 34
- 3.5 Cascaded Splitting Architecture for a 16-Emitter Array . . . 36

4 Thermo-Optic Phase Shifter Design 39
- 4.1 Phase Shifting Mechanisms for Optical Phased Arrays . . . 39
- 4.2 Temperature Dependence of the Effective Index . . . 40
- 4.3 Phase Shift Requirement and Heater Length Estimation . . . 42
- 4.4 Thermal Simulation and Power Analysis . . . 42
- 4.5 Final Heater Geometry and Design Trade-Off . . . 45

5 Emitter Design and Far-Field Analysis 47
5.1 Far-Field Formation in Optical Phased Arrays 47
5.2 Design of the One-Dimensional Emitter 49
5.3 Calibration of Optical Phased Arrays 52
5.4 Far-Field Analysis of the Designed Optical Phased Array 56
5.5 Imaging applications and random phase patterns 60

6 Conclusion 63

Bibliography 67

Chapter 1

Introduction

This chapter introduces the general context and motivation of the thesis. The discussion is initially focused on the relevance of beam steering and optical phased arrays in modern photonic systems, with particular attention to applications in the mid-infrared spectral region. The basic operating principle of integrated optical phased arrays is then outlined, highlighting the key concepts required to understand their behavior. Finally, the main architectural and technological aspects that influence the performance of mid-infrared optical phased arrays are discussed, providing the background necessary to frame the scope and objectives of this work.

1.1 Motivation and application context

The capability of dynamically controlling the direction of an optical beam is a fundamental requirement in a wide range of modern photonic systems. Beam steering is a key enabling function in applications such as free-space optical communications, remote sensing, spectroscopy, imaging systems, and light detection and ranging (LiDAR). In these scenarios, the steering mechanism is often required to operate with high angular resolution, fast response times, and long-term stability while maintaining a compact footprint and a high level of integration.

Traditionally, beam steering has been implemented using mechanical approaches based on rotating mirrors, galvanometric scanners, or micro-electromechanical systems (MEMS). Although these solutions are well established and capable of achieving wide steering angles, they inherently rely on moving parts, which introduce limitations in terms of speed, reliability, and scalability. Mechanical inertia restricts achievable scanning rates, while wear, alignment issues, and vibrations can negatively impact long-term stability. These drawbacks are increasingly critical in applications where compact, robust, and highly integrated systems are required [11].

In this context, Optical Phased Arrays (OPAs) have emerged as a promising solid-state alternative to mechanical beam steering systems. An OPA consists of an array of coherent optical emitters whose relative phases can be individually controlled. By exploiting constructive and destructive interference among the emitted optical fields, the far-field radiation pattern can be dynamically shaped and steered without any mechanical

motion. This approach enables fast beam reconfiguration, improved robustness, and compatibility with photonic integrated circuit technologies, making OPAs particularly attractive for scalable and integrated photonic platforms [4, 5].

In addition to beam steering and LiDAR applications, optical phased arrays have also recently attracted interest in computational imaging systems. By controlling the optical phase of multiple emitters, an OPA can generate spatially varying illumination patterns that can be used to probe a scene and reconstruct an image through computational methods. In particular, integrated photonic OPAs have been proposed as compact wavefront modulators for imaging systems based on multimode fibers. In these systems, the phases of the emitters are modulated to produce different speckle illumination patterns at the fiber output, which are then used to reconstruct an image of the target through single-pixel detection and numerical reconstruction algorithms [2]. Compared to conventional spatial light modulators, integrated OPAs offer the potential for significantly reduced system size and faster modulation speeds, making them attractive candidates for compact imaging platforms.

Although the concept of phased arrays was originally developed in the radio-frequency domain, its translation to the optical regime has opened new opportunities in integrated photonics. Near-infrared OPAs, primarily based on silicon photonics, have demonstrated the feasibility of compact beam steering systems compatible with mature fabrication processes. However, extending these concepts beyond the near-infrared toward longer wavelengths introduces additional challenges related to material properties, optical losses, and device scalability.

The mid-infrared (mid-IR) spectral region, typically defined between approximately 3 µm and 12 µm, has attracted increasing attention due to its relevance for a broad range of scientific and technological applications. In this wavelength range, many molecules exhibit strong and characteristic absorption features associated with fundamental vibrational modes, often referred to as the molecular fingerprint region. As a result, mid-IR photonics play a crucial role in applications such as chemical and gas detection, environmental monitoring, biomedical diagnostics, and security [4].

In addition to sensing, the mid-IR is also of significant interest for free-space optical systems, including thermal imaging and LiDAR. In these applications, solid-state beam steering solutions are particularly appealing, as they enable compact and robust systems that operate without mechanical scanning components. Recent works have shown that optical phased arrays can be successfully implemented in the mid-infrared, demonstrating beam steering capabilities on integrated photonic platforms [9].

Despite these opportunities, the realization of mid-IR OPAs remains a challenge. Material transparency, optical confinement, propagation losses, and thermal effects become increasingly critical at longer wavelengths, placing stringent constraints on both device design and platform selection. In particular, loss mechanisms associated with the guiding material and the underlying substrate can significantly affect the overall performance of integrated OPAs in the mid-infrared [7].

This thesis is positioned within this framework and focuses on the analysis and design of integrated optical phased arrays operating in the mid-infrared. By combining a system-level understanding of OPAs operation with a detailed investigation of the underlying

photonic components and technological constraints, the aim of this work is to provide insight into the key trade-offs that govern the performance of mid-IR OPAs and to support the development of efficient and scalable beam steering architectures.

1.2 Optical Phased Arrays: operating principle

An optical phased array is the photonic counterpart of a phased array system originally developed in the radio-frequency domain. Its operating principle relies on the coherent superposition of electromagnetic waves emitted by multiple spatially distributed radiating elements. By properly controlling the relative phase of each emitter, it is possible to shape and steer the overall radiation pattern without requiring any mechanical motion.

In an integrated photonic implementation, an optical phased array typically consists of a coherent optical source followed by a distribution network that splits the input signal into multiple branches. Each branch includes an individual phase control element and terminates with an emitting structure, such as a grating or an end-fire antenna. The optical fields radiated by the individual emitters interfere in the far field, resulting in a radiation pattern whose direction and shape depend on the imposed phase distribution throughout the array [4, 5]. An example of an integrated OPA architecture is shown in Fig. 1.1.

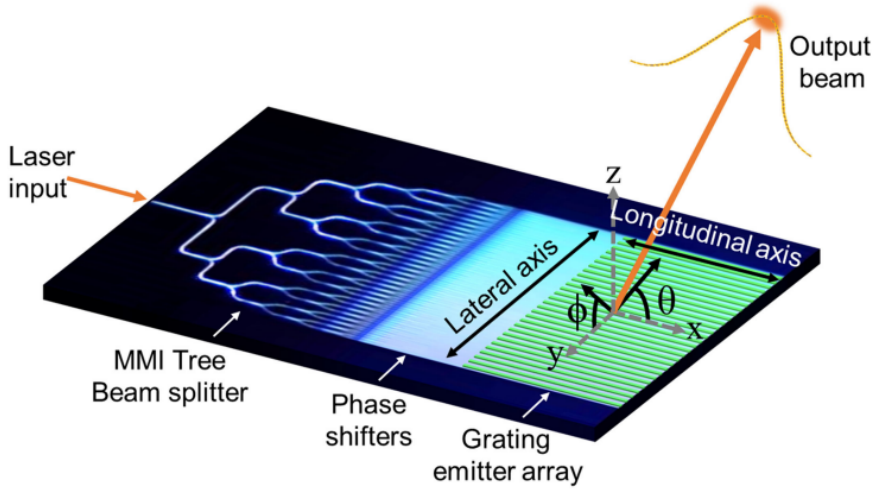

Figure 1.1: Schematic representation of an integrated optical phased array, including the optical distribution network, phase control elements and emitting structures (Reproduced from [9]).

From a physical standpoint, beam steering in an optical phased array is achieved by introducing a progressive phase shift between adjacent emitters. For a linear array with uniform spacing, a linear phase gradient results in constructive interference along a specific direction in the far field, corresponding to the steering angle of the main lobe. Changing the phase gradient allows for continuous steering of the beam within a certain

angular range, which is determined by the array geometry and the spacing between the emitting elements.

The radiation characteristics of an optical phased array are often described in terms of the array factor, which captures the contribution of the relative positions and phases of the emitters to the overall far-field pattern. While the exact analytical formulation of the array factor depends on the specific array configuration, it provides useful information on key performance aspects such as beam width, side-lobe level, and steering range. In practical integrated systems, deviations from ideal behavior arise due to non-uniform amplitude distribution, phase errors, and fabrication tolerances, all of which can significantly affect the resulting far-field response [5].

From a system perspective, the far-field radiation pattern of an optical phased array can be interpreted as the combined effect of the radiation characteristics of the individual emitting elements and the array factor associated with their spatial arrangement and relative phases. Although the array factor primarily determines the steering capability and the formation of the main lobe, the radiation pattern of the single emitter plays a crucial role in defining the overall field of view and the suppression of grating lobes. As a result, both the emitter design and the array architecture must be jointly considered when evaluating the output performance of an integrated optical phased array [3].

In addition to phase control, the amplitude of the optical signal delivered to each emitter plays an important role in determining the shape of the radiation pattern. Amplitude non-uniformities introduced by the splitter network or by propagation losses can lead to increased side-lobe levels and reduced beam efficiency. For this reason, the design of the power distribution network and the control of losses across the array are critical aspects in the realization of high-performance optical phased arrays.

Although the basic operating principle of an optical phased array is conceptually simple, its practical implementation on an integrated photonic platform involves a number of design trade-offs. The number of emitters, their spacing, the available phase tuning range, and the achievable phase resolution directly influence the steering performance and the complexity of the control system. These aspects become even more critical when optical phased arrays are implemented at mid-infrared wavelengths, where material properties and propagation losses impose additional constraints on device design.

In this work, the operating principles outlined in this section provide the foundation for the system-level analysis of mid-infrared optical phased arrays. Rather than focusing on a single monolithic simulation of the entire array, the behavior of the system is investigated through the analysis of its individual building blocks, allowing a clearer understanding of how component-level characteristics impact the overall far-field performance.

1.3 OPA Architectures and Their Impact on the Far-Field Response

When discussing the performance of an optical phased array, it is important to clarify what is meant by its output. Unlike many integrated photonic devices, whose output can be directly described in terms of optical power at a waveguide port, the output of an

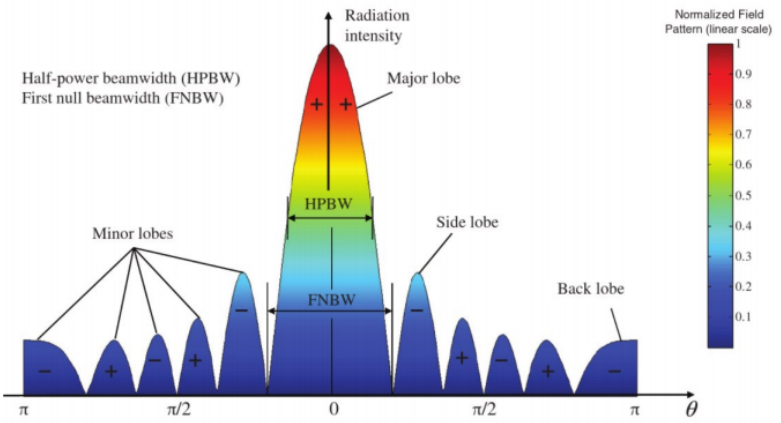

Figure 1.2: Representative far-field radiation pattern of an optical phased array, highlighting the main lobe, side lobes and beamwidth metrics commonly used to describe the spatial distribution of the emitted optical power (Reproduced from [5]).

OPA is defined by how light is distributed in space once it is radiated out of the chip. In other words, the relevant quantity is the far-field radiation pattern, which describes the direction, shape, and intensity of the emitted optical beam.

From an intuitive standpoint, the far-field pattern can be seen as the result of the interference between the optical waves emitted by the individual elements of the array. Depending on how these waves combine in space, light can be concentrated along a specific direction, spread over a wider angular region, or distributed among multiple secondary lobes. The ability to control this interference process is what enables beam steering and beam shaping in optical phased arrays [3, 5]. A representative example of a far-field radiation pattern and its main features is shown in Fig. 1.2.

Several factors influence the resulting far-field response. One of the most important features is the relative phase of the optical signals that feed the emitting elements. By introducing controlled phase differences across the array, the direction along which constructive interference occurs can be modified, allowing the main beam to be steered. In addition to phase control, the spatial arrangement of the emitters and their mutual spacing play a crucial role. These parameters determine how narrow the main beam can be and whether unwanted secondary beams, commonly referred to as side lobes or grating lobes, appear in the radiation pattern [3].

The characteristics of the far-field pattern are also influenced by the properties of the individual emitting elements. Each emitter radiates light according to its own angular distribution, which sets a natural limit to the overall field of view of the array. Consequently, the final output of an optical phased array results from the combined effect of the interference among emitters and the radiation properties of each individual element.

Based on the spatial arrangement of the emitting elements, optical phased arrays can be broadly classified as one-dimensional or two-dimensional. In a one-dimensional OPA, the emitters are arranged along a single line, and beam steering is achieved only within one angular plane. As a result, the beam can be scanned along a line but not over an area.

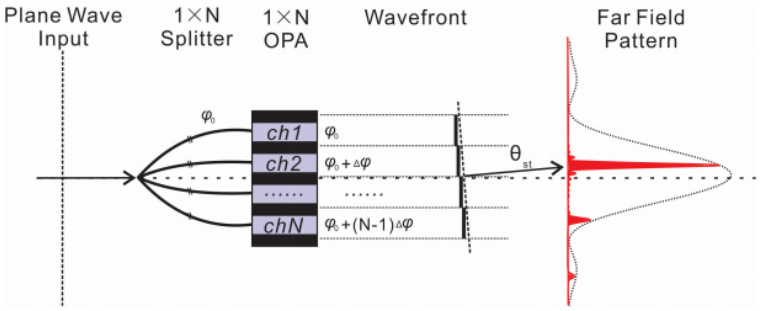

Figure 1.3: Conceptual illustration of beam steering in a one-dimensional optical phased array. A progressive phase shift applied across the array channels results in a tilted wavefront and in the steering of the main lobe along a single angular direction in the far field (Reproduced from [6]).

This configuration is often sufficient for applications where scanning is required along a single direction and is attractive because of its relative simplicity. The operating principle of beam steering in a one-dimensional optical phased array is schematically illustrated in Fig. 1.3.

In contrast, two-dimensional optical phased arrays employ a two-dimensional grid of emitters, enabling beam steering along both angular coordinates. This allows the beam to be scanned over a two-dimensional field of view, which is essential for applications such as imaging or three-dimensional sensing. However, the increased flexibility offered by two-dimensional OPAs comes at the cost of greater architectural complexity, as a larger number of emitters, control signals, and calibration procedures are required to achieve the desired output [3]. An illustrative example of two-dimensional beam steering enabled by a two-dimensional optical phased array is shown in Fig. 1.4.

In practical implementations, the ideal far-field response is often degraded by imperfections that affect the uniformity of the array. Variations in phase and amplitude among the emitters, caused by fabrication tolerances, propagation losses, or thermal effects, can distort the intended interference pattern. These non-idealities may lead to beam pointing errors and increased side-lobe levels, resulting in a noticeable difference between the theoretical and the measured output of an optical phased array [6].

For these reasons, a clear understanding of how architectural choices and component non-idealities influence the far-field response is essential for the design of reliable and scalable optical phased arrays. This perspective motivates a system-level analysis in which output performance is interpreted as the cumulative result of the behavior of individual building blocks, a concept that will be further developed in the following chapters.

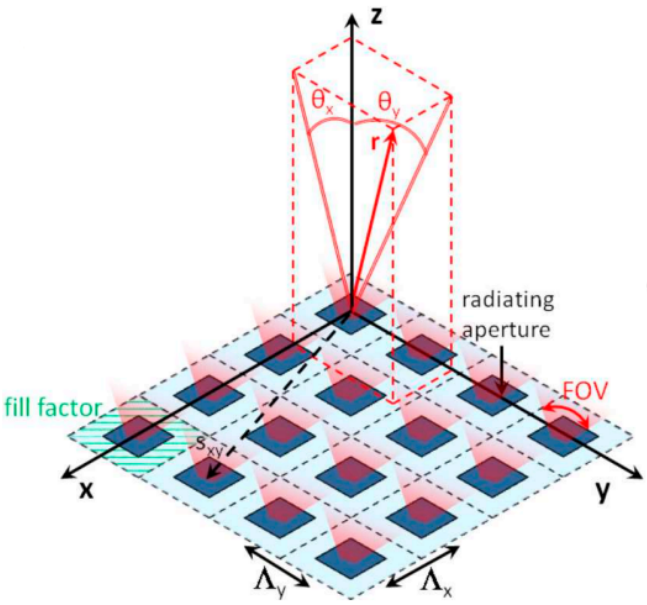

Figure 1.4: Schematic illustration of a two-dimensional optical phased array, where a two-dimensional arrangement of emitting elements enables beam steering along both angular coordinates, allowing scanning over a two-dimensional field of view (Reproduced from [3]).

1.4 Physical and Technological Limitations of Mid-Infrared OPAs

Although the operating principles of optical phased arrays are largely independent of the wavelength regime, their practical implementation is strongly influenced by the physical and technological constraints imposed by the underlying photonic platform. These constraints become particularly critical in the mid-infrared spectral region, where material properties, optical confinement, and propagation losses play a decisive role in determining device performance.

Silicon, which represents the dominant material platform for near-infrared integrated photonics, exhibits increasing optical absorption at wavelengths beyond approximately 8 µm due to multiphonon processes. This intrinsic limitation significantly restricts its applicability for mid-infrared optical phased arrays and motivates the exploration of alternative material platforms. Several solutions have been proposed, including suspended silicon waveguides, silicon–germanium alloys, and III–V compound semiconductors, each offering specific advantages and trade-offs in terms of transparency, fabrication complexity, and integration capability.

Among group-IV platforms, germanium-on-silicon has emerged as a particularly promising solution for mid-infrared integrated photonics. Germanium provides a wide transparency window that extends well into the mid-infrared while maintaining compatibility with silicon-based fabrication processes. Experimental demonstrations have shown that

Ge-on-Si waveguides can achieve effective light confinement and relatively low propagation losses in the wavelength range relevant for mid-infrared applications, enabling the realization of more complex integrated devices, including optical phased arrays [8, 9].

Despite these advantages, Ge-on-Si platforms are affected by several loss mechanisms that become increasingly relevant at longer wavelengths. In addition to intrinsic material absorption in germanium, optical losses can arise from modal overlap with the silicon substrate, as well as scattering induced by fabrication imperfections and defects at the Ge/Si interface. The contribution of these effects depends on both the waveguide geometry and the operating wavelength, leading to a non-negligible variation of propagation losses across the mid-infrared spectrum [7].

For optical phased arrays, such loss mechanisms have direct implications at the system level. Propagation losses and non-uniform attenuation across the distribution network introduce amplitude imbalances between array elements, which in turn affect the far-field radiation pattern by increasing side-lobe levels and reducing beam efficiency. Moreover, loss-induced heating and thermal gradients can indirectly impact phase control, further contributing to deviations from the ideal steering behavior discussed in the previous section.

These considerations highlight the importance of accounting for physical and technological limitations already at the design stage of mid-infrared optical phased arrays. In particular, the choice of material platform and waveguide geometry must be carefully balanced against architectural requirements, such as array size and phase control resolution. In this context, a simulation-driven and component-oriented analysis becomes an essential tool to assess the impact of material losses and technological constraints on the overall performance of integrated mid-infrared OPAs.

1.5 Simulation Tools and Numerical Methods

The design and analysis of the optical phased array presented in this work rely extensively on numerical simulations. Integrated photonic devices involve complex electromagnetic interactions that cannot be accurately predicted using analytical models alone, especially when considering realistic geometries and material properties. For this reason, different numerical tools available in the RSoft photonic simulation suite have been employed throughout the thesis.

In particular, three main simulation environments have been used: BeamPROP, FullWAVE, and FemSIM. Each of these tools relies on a different numerical approach and is therefore suited for specific types of analyses. BeamPROP is mainly used for the simulation of light propagation along photonic structures, FullWAVE provides a full electromagnetic solution of Maxwell's equations, and FemSIM is employed to compute the modal properties of waveguides. The combined use of these methods makes it possible to analyze both the propagation behavior of the optical field and the modal characteristics of the waveguide structures.

1.5.1 BeamPROP

BeamPROP is a simulation tool based on the Beam Propagation Method (BPM), which is widely used for modeling the propagation of optical fields in guided-wave structures. The BPM approach assumes that the optical field mainly propagates along a dominant direction and computes the evolution of the electromagnetic field along this axis. This approximation significantly reduces the computational complexity of the problem, allowing the simulation of relatively large photonic circuits.

In BeamPROP the propagation of the optical field is calculated by solving a paraxial approximation of the Helmholtz equation. The structure is divided into small propagation steps along the main direction of propagation, and the optical field is iteratively updated as it advances through the device. This approach makes the method particularly efficient for analyzing long photonic structures such as waveguides, splitters, and optical distribution networks.

In this thesis BeamPROP has been extensively used to simulate the propagation of the optical field through the different components of the optical phased array. In particular, it has been employed to analyze the power distribution in the splitting network and to evaluate the propagation of the optical field through the array of emitters. The main advantage of this method is the relatively low computational cost, which allows the simulation of large structures containing multiple photonic elements.

However, since BPM relies on the assumption of predominantly forward propagation, it cannot fully capture effects such as strong back reflections or complex scattering phenomena. For this reason, more rigorous electromagnetic solvers are required when a full solution of Maxwell's equations is needed.

A typical example of optical field propagation simulated with BeamPROP is reported in Fig. 1.5.

1.5.2 FullWAVE

FullWAVE is a rigorous electromagnetic simulation tool based on the Finite-Difference Time-Domain (FDTD) method. Unlike BPM-based approaches, FDTD directly solves Maxwell's equations in both space and time, providing a full electromagnetic description of the propagation of optical waves.

In the FDTD method the simulation domain is discretized into a spatial grid, and the electric and magnetic fields are calculated at each point of the grid as a function of time. The fields are updated iteratively using the discretized form of Maxwell's equations, allowing the electromagnetic wave to propagate through the simulated structure. This approach makes it possible to model complex optical phenomena such as reflections, scattering, and radiation effects.

Due to its rigorous nature, FullWAVE provides highly accurate results and is particularly suitable for analyzing structures where the assumptions of BPM are no longer valid. In the context of this thesis, FullWAVE has been used to validate specific aspects of the waveguide design and to evaluate the propagation losses of the optical modes in the germanium-on-silicon platform.

The main limitation of the FDTD method is its high computational cost. Since the

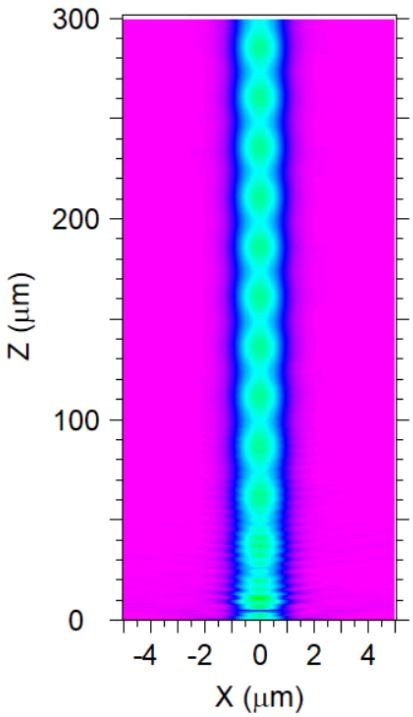

Figure 1.5: Optical field propagation along a Ge-on-Si waveguide simulated using BeamPROP. The Beam Propagation Method provides an efficient description of the field evolution along the main propagation direction.

entire simulation domain must be discretized in three dimensions and the fields must be updated at every time step, the required computational resources increase significantly with the size of the simulated structure. For this reason, FullWAVE is typically used for the analysis of smaller sections of the photonic circuit rather than for the simulation of the complete optical phased array.

An example of electromagnetic field distribution computed with the FullWAVE solver is shown in Fig. 1.6.

1.5.3 FemSIM

FemSIM is a simulation tool used to compute the modal properties of optical waveguides using a finite-element method (FEM) formulation. In contrast to BeamPROP and FullWAVE, which simulate the propagation of electromagnetic fields through photonic structures, FemSIM is specifically designed to calculate the guided modes supported by a waveguide geometry.

The finite-element method discretizes the cross section of the waveguide into small elements and solves the eigenvalue problem derived from Maxwell's equations. This procedure allows the determination of the spatial distribution of the electromagnetic field associated with each guided mode, together with the corresponding effective refractive index.

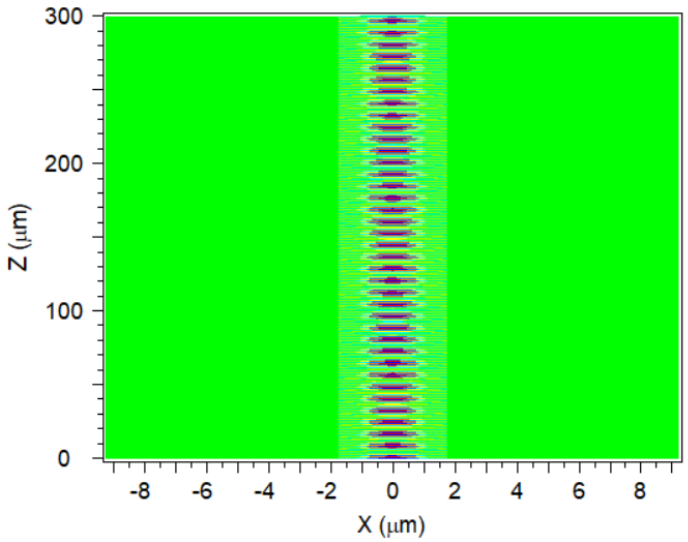

Figure 1.6: Contour map of the magnetic field component H_y obtained using the FullWAVE FDTD solver. This method provides a full electromagnetic solution of Maxwell's equations and can capture effects such as reflections, scattering, and non-paraxial propagation.

In this work FemSIM has been used to analyze the modal properties of the germanium-on-silicon waveguides forming the optical phased array. In particular, it has been employed to evaluate the effective refractive index of the first guided modes and to study the modal confinement as a function of the waveguide geometry. These simulations played an important role in the selection of the waveguide dimensions adopted in the final design.

The modal analysis provided by FemSIM also allows the visualization of the spatial distribution of the optical field within the waveguide cross section, offering a clear understanding of how the electromagnetic energy is confined inside the germanium core.

An example of modal analysis performed with FemSIM is shown in Fig. 1.7, where the three components of the electric field of the fundamental mode are reported.

Comparison of the simulation methods The three simulation tools described above provide complementary information and were selected according to the specific physical problem under investigation. FemSIM is particularly suited for the analysis of the guided modes supported by a given waveguide cross section, since it directly provides the effective refractive indices and the field distribution of the eigenmodes. For this reason, it was used in this work to study modal confinement and to define the final waveguide geometry.

BeamPROP, on the other hand, offers an efficient way to simulate the propagation of optical fields along integrated photonic structures. Its reduced computational cost makes it especially convenient for the analysis of relatively large devices such as splitters and complete distribution networks. In this thesis, BeamPROP was therefore used to study the propagation of the optical field in the splitting stage and in the full OPA architecture.

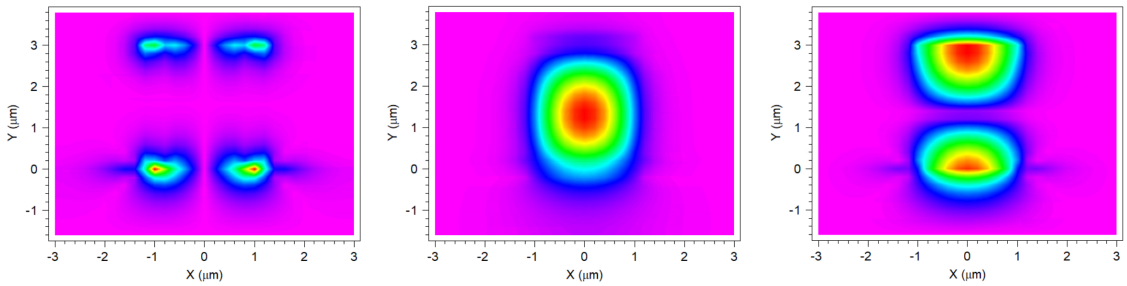

(a) E_x (b) E_y (c) E_z

Figure 1.7: Electric field components of the fundamental mode of the Ge-on-Si waveguide computed using the FemSIM eigenmode solver. The plots show the spatial distribution of the three components of the electric field in the waveguide cross section.

However, BeamPROP is based on a predominantly forward-propagating approximation, which may become less accurate in structures where the field evolution significantly deviates from a single propagation direction. This can occur, for example, in strongly curved sections or in S-bend geometries characterized by a non-negligible horizontal offset. In such cases, the optical field may experience effects that are not fully captured by a unidirectional beam propagation method.

For these situations, FullWAVE provides a more rigorous solution, since it directly solves Maxwell's equations without relying on a preferred propagation direction. Although this method is computationally much more demanding, it is more suitable for the analysis of structures where reflections, radiation effects, or non-paraxial propagation may play a relevant role.

Overall, the use of these three tools enabled a balanced simulation strategy in which each method was employed according to its strengths: FemSIM for modal analysis, BeamPROP for efficient field propagation in extended structures, and FullWAVE for more rigorous electromagnetic validation of critical geometries.

A comparison between the two propagation approaches is shown in Fig. 1.8 for the case of an S-bend waveguide. Such structures are characterized by a non-negligible horizontal offset, which may lead to deviations from a purely unidirectional propagation regime.

In these situations the Beam Propagation Method may lose part of the physical information associated with reflections or non-paraxial components of the electromagnetic field. FullWAVE, on the other hand, directly solves Maxwell's equations and therefore provides a more accurate representation of the electromagnetic field distribution, although at the cost of significantly higher computational resources.

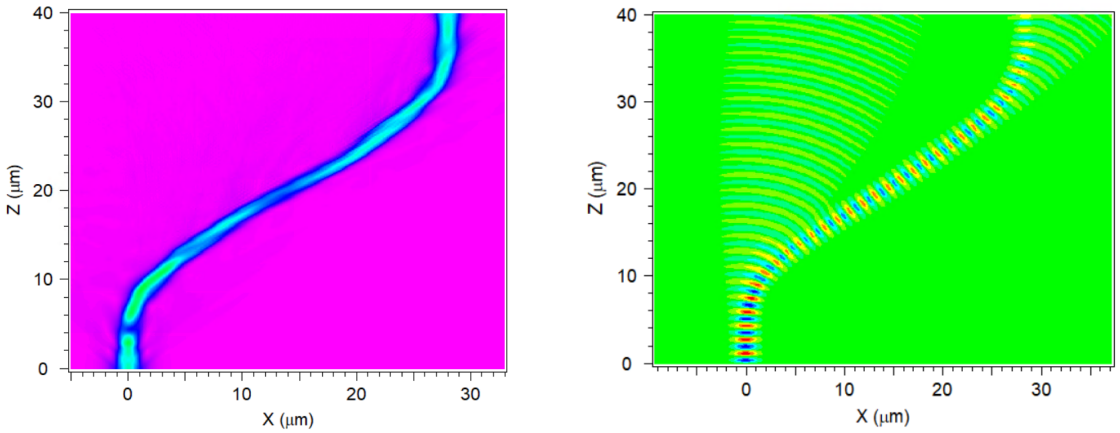

(a) BeamPROP simulation

(b) FullWAVE simulation

Figure 1.8: Comparison between BeamPROP and FullWAVE simulations for an S-bend waveguide. BeamPROP efficiently models the propagation of the optical field along the device using a unidirectional approximation, while FullWAVE provides a full electromagnetic solution of Maxwell's equations, allowing a more accurate description of the field evolution in strongly curved geometries.

1.6 Scope and structure of the thesis

The aim of this thesis is the design and numerical analysis of an integrated optical phased array (OPA) operating in the mid-infrared spectral region on a germanium-on-silicon photonic platform. Particular attention is devoted to the investigation of the main building blocks required for the realization of a fully integrated OPA, including the waveguide platform, the optical power distribution network, the thermo-optic phase shifters, and the emitting array responsible for the generation of the far-field radiation pattern. The study focuses on the wavelength range between 4 μm and 8 μm, which is particularly relevant for sensing and LiDAR applications in the mid-infrared.

The thesis is organized as follows.

Chapter 2 presents the design and analysis of the waveguide platform. The optical properties of germanium in the considered wavelength range are first discussed, and a realistic loss model is implemented within the simulation environment. Based on this model, the geometry of the Ge-on-Si strip waveguide is optimized by analyzing the effective indices of the guided modes. The routing of the optical signals within the circuit is also investigated through a comparison of different waveguide bending solutions.

Chapter 3 focuses on the design of the optical power distribution network. Two alternative splitting architectures, namely Y-splitters and multimode interference (MMI) couplers, are analyzed and compared. After evaluating their performance over the operating wavelength range, the final splitting network is implemented using cascaded 1×2 MMI couplers to distribute the optical power to the emitters of the array.

Chapter 4 addresses the design of the thermo-optic phase shifting mechanism used to control the phase of the optical signals in each branch of the array. The dependence of

the effective refractive index on temperature is analyzed, and the heater length required to achieve the desired phase shift is estimated. Thermal simulations are then performed to evaluate the temperature distribution and to investigate the effect of thermal isolation trenches.

Chapter 5 presents the design of the emitting array and the analysis of the resulting far-field radiation pattern. The influence of the emitter spacing and the number of emitters on the array performance is discussed. A phase calibration strategy is implemented to correct phase mismatches arising from different optical path lengths, and the steering capability of the optical phased array is evaluated through far-field simulations. In addition, the response of the array under random phase configurations is investigated, highlighting the possibility of generating complex optical patterns that can be exploited in imaging and computational sensing applications.

Finally, Chapter 6 summarizes the main results of the work and discusses possible directions for future developments of mid-infrared optical phased array systems.

Chapter 2

Waveguide Design for Mid-Infrared Optical Phased Arrays

This chapter is devoted to the design and analysis of the optical waveguide that constitutes the fundamental building block of the optical phased array investigated in this thesis. Since all functional components of an integrated OPA, such as power splitters, phase shifters, and optical emitters, operate in guided modes, the choice of waveguide platform and geometry plays a central role in determining the overall performance of the system.

The analysis focuses on the Ge-on-Si photonic platform, which has emerged as a promising solution for mid-infrared integrated photonics due to its favorable optical properties and compatibility with silicon-based fabrication processes. Particular attention is devoted to the material characteristics of germanium in the mid-infrared spectral range, including refractive index dispersion and optical loss mechanisms because these factors directly influence modal confinement and propagation behavior.

In order to translate the physical properties discussed in the literature into a practical design framework, numerical simulations are employed throughout the chapter. The adopted modeling approach is described in detail, with an emphasis on the assumptions introduced to balance physical accuracy and computational efficiency. Based on this framework, the waveguide cross-section is defined by selecting appropriate geometrical parameters that ensure single-mode operation and adequate confinement of the fundamental mode over the wavelength range of interest.

Finally, the impact of waveguide curvature is analysed, since curved sections are unavoidable in realistic integrated layouts and impose additional constraints on loss and footprint. The chapter concludes with the definition of a final reference waveguide geometry, which is used consistently in the subsequent chapters for the design and analysis of power splitters, phase shifters, and optical emitters.

2.1 Germanium-on-Silicon Material Platform

The development of integrated optical phased arrays operating in the mid-infrared requires a material platform that simultaneously provides optical transparency over a broad spectral range, strong modal confinement, and compatibility with scalable fabrication processes. Among the available solutions, the germanium-on-silicon (Ge-on-Si) platform has attracted significant attention in recent years as a viable compromise between optical performance and technological maturity.

Germanium exhibits a relatively high refractive index throughout the mid-infrared spectral range, enabling tight optical confinement when combined with lower-index surrounding materials. When germanium is integrated on a silicon substrate, this index contrast allows the realization of compact waveguide geometries capable of supporting guided modes with a limited footprint, which is a key requirement for dense photonic integration. At the same time, the use of silicon as a supporting substrate leverages well-established fabrication processes, making Ge-on-Si particularly attractive for large-scale integration and reproducibility [4, 9].

Ge-on-Si waveguides have been successfully employed in several mid-infrared integrated photonic devices, including optical phased arrays for beam steering applications. Experimental demonstrations reported in the literature show that this platform can sustain guided propagation over wavelengths extending from the short-wave infrared to the mid-infrared region while maintaining propagation losses compatible with practical on-chip applications [8, 9]. These results have motivated its adoption as a reference platform for mid-infrared OPA implementations.

Despite these advantages, the Ge-on-Si platform also presents intrinsic limitations that must be taken into account during the design phase. In particular, the silicon substrate introduces additional absorption at longer wavelengths due to multiphonon processes, which can increase the effective propagation loss when a significant fraction of the optical mode extends into the substrate. As discussed in the literature, this effect becomes increasingly relevant in the upper portion of the mid-infrared range and is strongly influenced by the modal confinement provided by the waveguide geometry [7, 8].

For these reasons, the choice of a Ge-on-Si platform does not solely rely on material properties but must be accompanied by a careful waveguide design aimed at maximizing modal confinement within the germanium core while minimizing overlap with lossy regions. In the context of optical phased arrays, where multiple components are cascaded and curved routing sections are unavoidable, this balance is particularly critical. The Ge-on-Si platform therefore represents a suitable but non-trivial starting point whose effective performance depends on both material characteristics and geometrical optimization.

2.2 Optical Properties of Germanium in the Mid-Infrared

A correct description of the optical properties of germanium in the mid-infrared spectral range is essential for the design of integrated waveguides and, more generally, for the evaluation of the performance of Ge-on-Si photonic circuits. In this wavelength region, germanium combines a high refractive index with a relatively wide transparency window,

making it suitable for strong modal confinement while supporting operation beyond the near-infrared regime.

The real part of the refractive index of germanium exhibits moderate but non-negligible dispersion across the mid-infrared. Experimental data reported in the literature show that the exact wavelength dependence of the refractive index may vary depending on the quality of the material, growth conditions, and measurement techniques. As a consequence, the refractive index is typically described through empirical models or tabulated values rather than by a single constant parameter [4, 8]. This dispersion must be taken into account when analyzing waveguide behavior over a broad spectral range since it directly influences the modal confinement and effective index values.

In addition to dispersion, optical losses represent a critical aspect of germanium-based waveguides. At the material level, absorption in germanium remains relatively low over a significant portion of the mid-infrared, enabling guided propagation with acceptable attenuation. However, when germanium is integrated on a silicon substrate, additional loss mechanisms arise that are not intrinsic to the germanium core itself. In particular, absorption in the silicon substrate becomes increasingly relevant at longer wavelengths due to multiphonon processes, leading to an increase in the effective propagation loss when the optical mode extends significantly into the substrate [7, 9].

For this reason, the losses commonly reported for Ge-on-Si waveguides should be interpreted as effective losses, resulting from the combined contributions of material absorption, substrate leakage, and scattering at the waveguide interfaces. These losses are therefore not purely material constants but depend on the spatial distribution of the guided mode, which is in turn determined by the waveguide geometry. As highlighted in several studies, variations in waveguide dimensions can significantly alter the overlap of the optical mode with lossy regions, leading to measurable differences in propagation loss even for nominally identical material systems [7, 8].

From a design perspective, this distinction between intrinsic material properties and geometry-dependent effective losses is particularly important. While material dispersion and absorption set fundamental limits on achievable performance, the waveguide cross-section offers an additional degree of freedom to mitigate loss through enhanced confinement within the germanium core. In the context of optical phased arrays, where light propagates through multiple cascaded components and curved routing sections, controlling these effects is essential to preserve optical power and phase integrity across the array. Consequently, a realistic waveguide design must account for both the wavelength-dependent optical properties of germanium and their interplay with waveguide geometry.

2.3 Numerical Modeling in RSoft

The numerical modeling strategy adopted in this work aims to obtain a waveguide description that is both physically meaningful and consistent with experimentally reported Ge-on-Si propagation losses in the mid-infrared. This step is necessary because the default material models available in commercial simulation tools do not fully capture the loss behavior of germanium beyond the near-infrared region. As a consequence, a direct use of the built-in material database would lead to an unrealistically optimistic representation

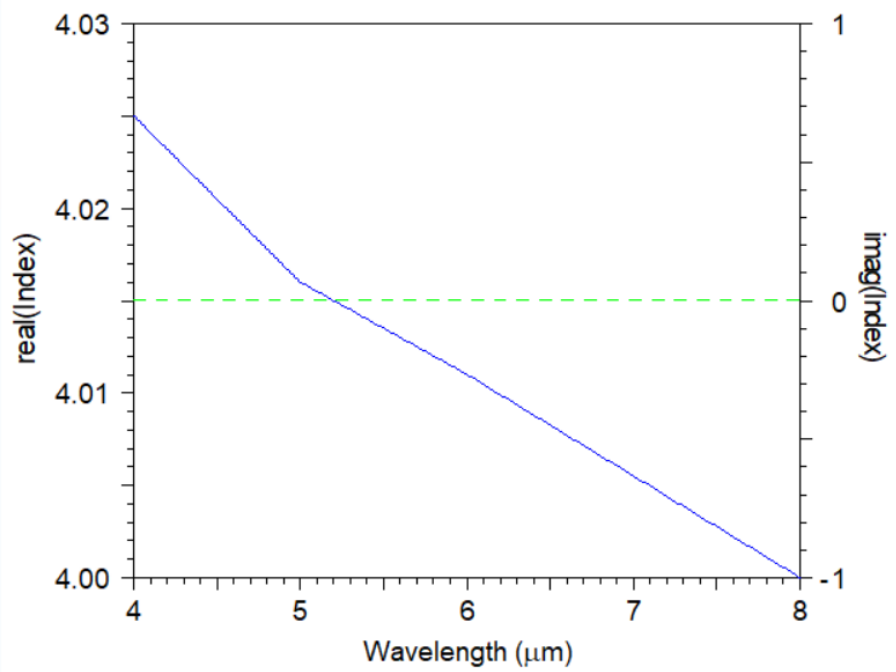

Figure 2.1: Real (solid line) and imaginary (dashed line) parts of the refractive index of germanium as implemented by default in the RSoft material database over the 4–8 µm wavelength range.

of waveguide performance in the wavelength range of interest.

The target structure considered throughout this study is a Ge-on-Si strip waveguide with air upper cladding, operating between 4 µm and 8 µm. Figure 2.1 reports the real and imaginary parts of the germanium refractive index as implemented by default in RSoft. While the real part exhibits a dispersive behavior over a broad wavelength range, the imaginary part is defined only up to approximately 2 µm, resulting in vanishing material losses at longer wavelengths. This limitation motivates the need for a dedicated loss modeling procedure.

Before introducing loss calibration, an initial waveguide geometry must be defined. The waveguide height is fixed at 3 µm according to the fabrication constraints specified by the CORNERSTONE Ge-on-Si wafer process [1]. This choice represents a hard technological constraint and ensures that the simulated structure remains compatible with a realizable fabrication platform. The waveguide width, on the other hand, is treated as a free design parameter and is selected through a preliminary modal confinement study.

The width selection is based on the analysis of the effective index of the guided modes as a function of the waveguide width. This study is primarily driven by the real part of the effective index and by the spatial distribution of the modal field, which determine the degree of confinement within the germanium core and the separation between the fundamental mode and higher-order modes. Although the default RSoft loss model does not accurately represent mid-infrared attenuation, this limitation does not significantly affect the relative comparison of modal confinement across different widths. The effective

index is therefore computed for wavelengths $\lambda = 4$ µm, 6 µm, and 8 µm over a width range between 2 µm and 4 µm. The resulting trends are reported in Fig. 2.2. Based on these results, a width of 2 µm is selected, as it provides strong confinement of the fundamental mode and a clear separation from the next supported mode across the considered wavelength range.

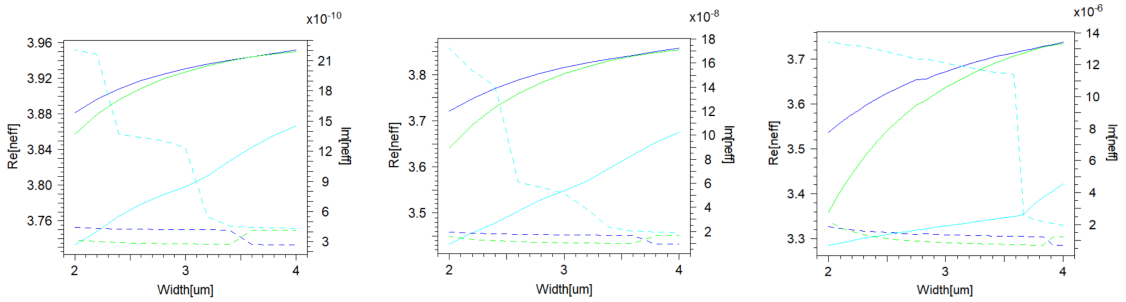

(a) $\lambda = 4$ µm (b) $\lambda = 6$ mum (c) $\lambda = 8$ µm

Figure 2.2: Real (solid lines) and imaginary (dashed lines) parts of the effective index as a function of waveguide width for the first three guided modes. Blue curves correspond to mode 0, green curves to mode 1, and cyan curves to mode 2. Figures (a), (b), and (c) refer to wavelengths of 4 µm, 6 µm, and 8 µm, respectively.

Once a reference waveguide geometry is established, experimentally reported propagation losses are used to calibrate the numerical model. In the literature, Ge-on-Si losses are typically reported as effective waveguide losses in decibel per centimeter at specific wavelengths and for selected waveguide thicknesses. The values adopted in this work are summarized in Table 2.1, together with the corresponding references [7, 8]. Since these losses already include the combined effects of material absorption, scattering, and substrate interaction, they are more naturally associated with modal attenuation rather than with a purely intrinsic material property.

Table 2.1: Ge-on-Si waveguide propagation losses reported in the literature for mid-infrared wavelengths.

Wavelength [µm]	Waveguide height [µm]	Loss [dB/cm]	Reference
3.8	3	0.6	[7]
7.5	3	2.5	[7]
8.5	3	20	[8]

The reported loss values are first converted into an equivalent imaginary part of the modal effective index, $\Im\{n_{\text{eff}}\}$. Using FEMSIM, the complex effective index of the guided mode is then computed, and the imaginary part of the germanium refractive index is adjusted until the simulated $\Im\{n_{\text{eff}}\}$ matches the target value derived from the literature. This calibration procedure is repeated for all wavelengths for which experimental data are available. Since the reported loss values cover only a limited set of wavelengths,

interpolation is employed to assign physically consistent loss values at intermediate wavelengths. In this work, a smooth interpolation performed in MATLAB is used to extend the definition of the imaginary refractive index over the full 4-8 µm range, ensuring the continuity of the material model.

The final complex refractive index adopted for germanium, including the modified imaginary part used in the simulations, is shown in Fig. 2.3. This approach yields a waveguide model that simultaneously satisfies fabrication constraints and reproduces experimentally observed loss levels. The resulting calibrated waveguide definition is employed in the following sections to analyze waveguide behavior and to define a final reference geometry for the design of the optical phased array components.

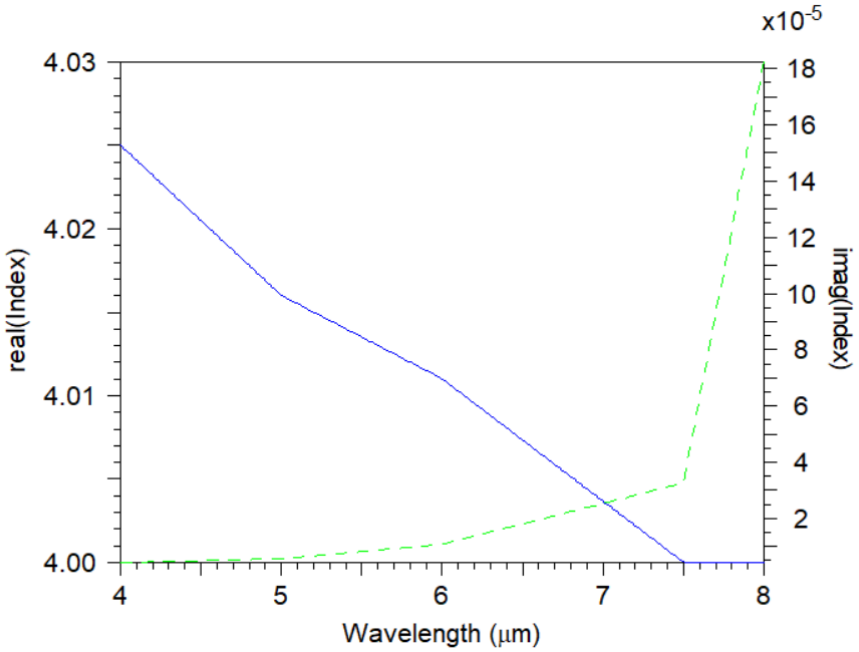

Figure 2.3: Real (solid line) and imaginary (dashed line) parts of the refractive index of germanium adopted in the numerical simulations after loss calibration, over the 4–8 µm wavelength range.

2.4 Waveguide Geometry Definition

The definition of the waveguide geometry represents a key design step, as it directly affects modal confinement, propagation losses, and the overall scalability of the integrated photonic circuit. In this section, the waveguide width is selected based on a modal analysis performed using the calibrated material model introduced in Sec. 2.3.

Starting from the fixed waveguide height of 3 µm, imposed by fabrication constraints, the effective indices of the first guided modes are computed as a function of the waveguide width. Unlike the preliminary study discussed in the previous section, this analysis is carried out using the modified complex refractive index of germanium, which accounts for

mid-infrared propagation losses. This ensures that the resulting trends are representative of realistic operating conditions in the $4 - 8$ µm wavelength range.

The effective index is evaluated for waveguide widths ranging from 2 µm to 4 µm and for representative wavelengths within the operating band. The resulting curves show that increasing the waveguide width enhances modal confinement but also reduces the separation between the fundamental mode and higher-order modes. From a design perspective, this trade-off is particularly relevant, as a clear modal separation is required to ensure robust single-mode operation across the entire wavelength range of interest.

Based on this analysis, a waveguide width of 2 µm is selected. This value provides a favorable balance between strong confinement of the fundamental mode and sufficient separation from the next supported mode while avoiding unnecessarily large cross-sections that would compromise integration density. The corresponding results of the effective index analysis are reported in Fig. 2.4, where the updated material model is used for all simulations.

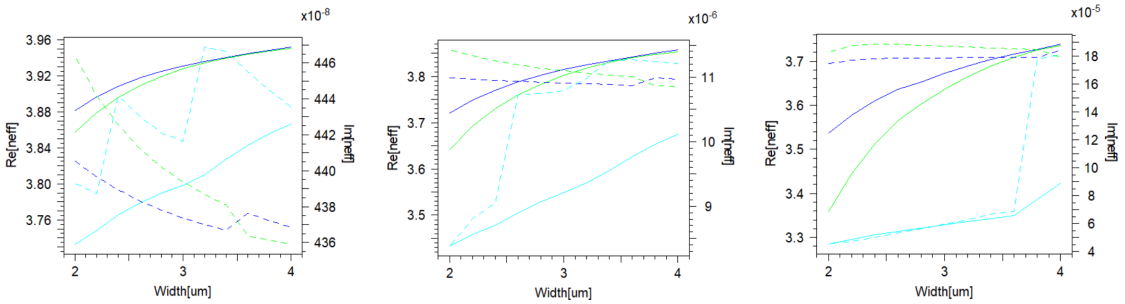

(a) $\lambda = 4$ µm (b) $\lambda = 6$ µm (c) $\lambda = 8$ µm

Figure 2.4: Real (solid lines) and imaginary (dashed lines) parts of the effective index as a function of waveguide width for the first three supported modes, computed using the calibrated complex refractive index of germanium. Blue curves correspond to mode 0, green curves to mode 1, and cyan curves to mode 2. Figures (a), (b), and (c) refer to wavelengths of 4 µm, 6 µm, and 8 µm, respectively.

The selected width represents an optimal compromise for mid-infrared operation and constitutes the basis for the subsequent analysis of curved waveguides and for the definition of a final reference geometry.

To further illustrate the modal confinement of the selected waveguide geometry, the distribution of the optical power flow associated with the fundamental guided mode is shown in Fig. 2.5. The plot represents the longitudinal component of the Poynting vector (Sz) obtained from the FEMSIM modal analysis.

2.5 Curved Waveguides and Bending Constraints

2.5.1 Circular Arc

Once the cross section of the waveguide has been selected, this information can be used to numerically calculate the best circular and bending parameters.

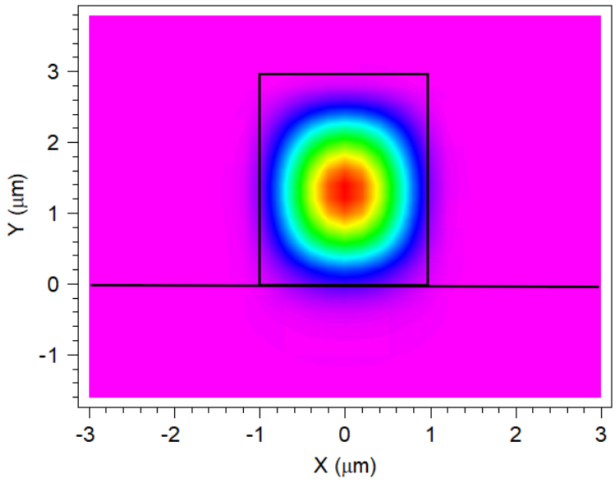

Figure 2.5: Power flow distribution (Sz) of the fundamental guided mode computed with FEMSIM at $\lambda = 6$ µm. The optical power is strongly confined within the germanium core.

A circular bend with a fixed 90° angle is first considered. The bending radius is varied between 10 µm and 120 µm in order to evaluate the trade-off between footprint and radiation loss.

The corresponding insertion loss is reported in Fig. 2.6.

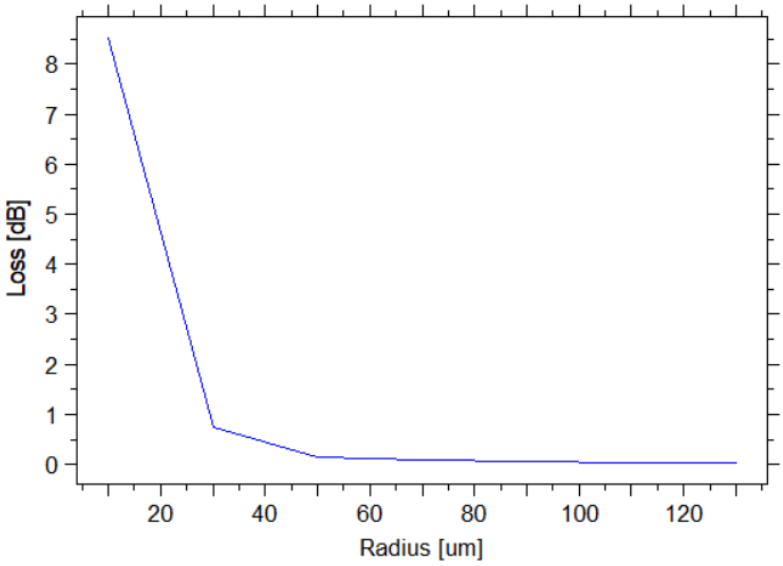

Figure 2.6: Insertion loss of a 90° circular bend as a function of the bending radius at 6 µm. Losses decrease significantly for radii larger than approximately 70 µm.

As expected, small radii lead to significant radiation losses due to insufficient modal confinement in the curved region. The losses remain high up to approximately 50 µm

radius, while for radii larger than about 70 µm they become negligible.

Although large radii provide low-loss performance, the circular arc introduces important layout constraints. Each routing step between splitting stages would require two consecutive 90° bends, increasing the overall footprint. Moreover, the radius imposes a geometric constraint on the horizontal spacing between waveguides, limiting flexibility to define the pitch required in the thermal modulation region.

2.5.2 S-Bend Configurations

In order to overcome the geometrical limitations of circular arcs, S-bend configurations are investigated. Two profiles available in RSoft are analyzed: the cosine S-bend and the raised-sine S-bend.

Two representative horizontal displacements between input and output waveguides are considered: 118 µm and 56 µm. For each case, the vertical length of the S-bend is varied in order to evaluate its impact on insertion loss. For the 118 µm displacement, the S-bend length is swept from 70 µm to 400 µm, while for the 56 µm displacement, it is varied from 70 µm to 200 µm.

The results are shown in Fig. 2.7. In both displacement cases, the raised-sine profile consistently exhibits lower losses compared to the cosine profile, particularly for shorter S-bend lengths. This behavior can be attributed to the smoother curvature transition of the raised-sine geometry, which reduces abrupt changes in the effective propagation direction and therefore limits radiation losses.

Beyond the purely numerical comparison, the S-bend solution provides a significant architectural advantage. Unlike circular arcs, the vertical length of the raised-sine S-bend can be adjusted according to the required horizontal displacement, allowing low-loss operation without being constrained by a fixed bending radius.

In addition, the use of S-bends avoids the need for two consecutive arcs at each routing step, reducing the overall footprint of the feeding network. Most importantly, it removes geometrical constraints on the final waveguide spacing, which is particularly relevant in the thermal modulation region where the pitch between adjacent waveguides must be carefully controlled.

For these reasons, the raised-sine S-bend is selected as the reference routing element for all subsequent stages of the OPA design.

2.6 Final Waveguide Geometry

Based on the analysis presented in the previous sections, the final waveguide configuration adopted for the OPA platform can be summarized as follows.

The material system consists of a Ge-on-Si strip waveguide with air upper cladding, operating in the mid-infrared range between 4 µm and 8 µm. The waveguide height is fixed to 3 µm according to the CORNERSTONE design rules [1], ensuring compatibility with the fabrication platform and sufficient vertical confinement. The width of the waveguide is set to 2 µm, as determined from the study of modal confinement, which guaranties strong fundamental-mode confinement and adequate separation from higher-order modes.

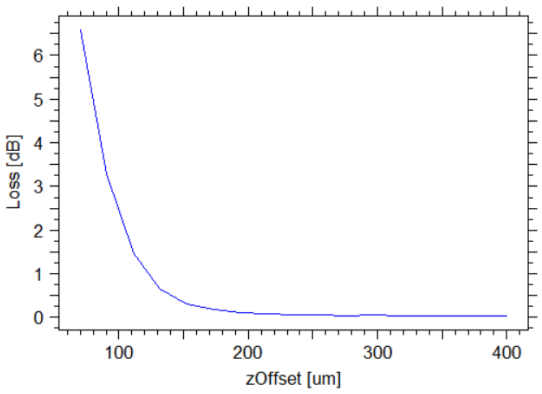

(a) Cosine S-bend, horizontal displacement 118 µm.

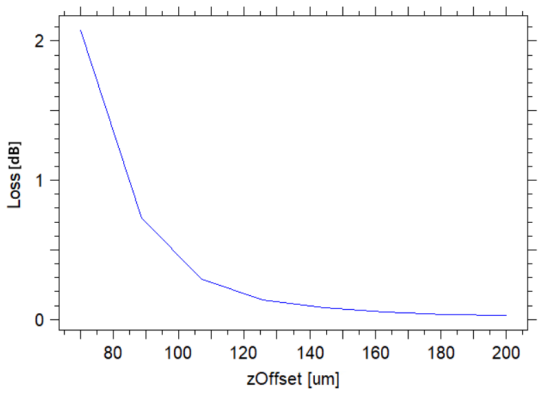

(b) Cosine S-bend, horizontal displacement 56 µm.

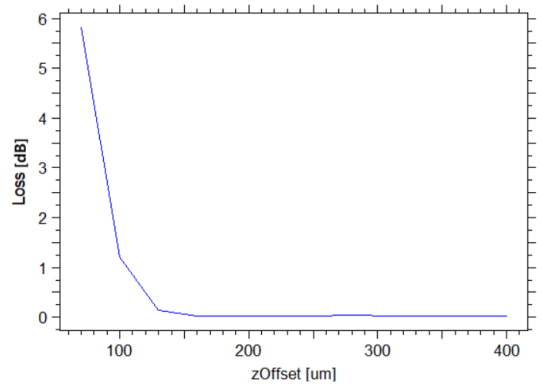

(c) Raised-sine S-bend, horizontal displacement 118 µm.

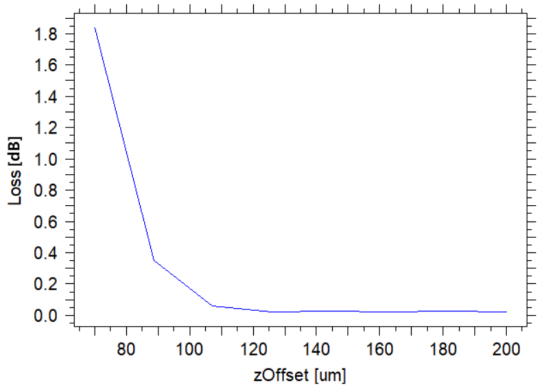

(d) Raised-sine S-bend, horizontal displacement 56 µm.

Figure 2.7: Insertion loss comparison between cosine and raised-sine S-bend profiles at 6 µm for two representative horizontal displacements. For both displacements, the raised-sine configuration provides lower losses for shorter S-bend lengths, while both profiles converge to negligible losses for sufficiently long transitions.

Material losses are incorporated by adjusting the imaginary part of the germanium refractive index to match the experimentally reported waveguide attenuation values. This ensures that the simulated effective index and propagation losses are consistent with data from the literature over the operating wavelength range.

For routing between functional blocks, the raised-sine S-bend configuration is selected. Compared to circular arcs and cosine S-bends, this profile provides lower bending losses for practical routing lengths while offering greater flexibility in defining the horizontal displacement between waveguides. This choice avoids geometrical constraints on the pitch in the thermal modulation region and reduces the overall footprint of the device.

Unless otherwise specified, all subsequent simulations are performed at the central wavelength of 6 µm and consider the fundamental guided mode (mode 0). The geometrical and material parameters defined in this chapter constitute the reference platform for the

design of the splitting, phase-shifting, and emission stages of the optical phased array.

The main geometrical elements adopted in the final design are illustrated in Fig. 2.8, which shows both the cross section of the Ge-on-Si strip waveguide and the raised-sine S-bend used for routing between functional blocks.

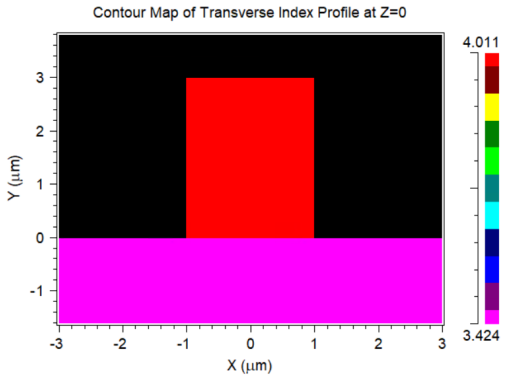

(a) Cross-sectional geometry of the Ge-on-Si strip waveguide.

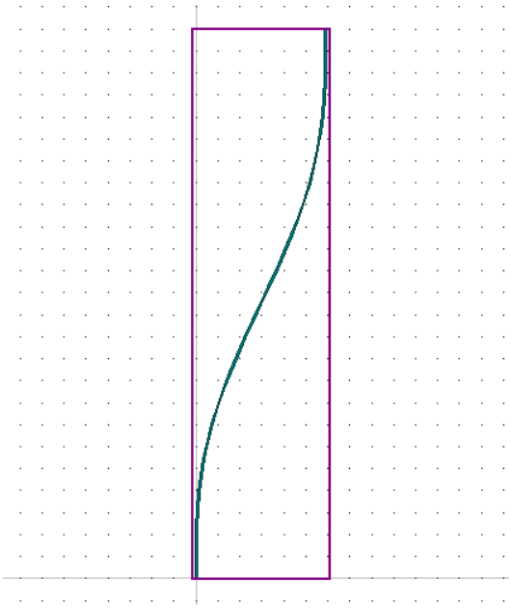

(b) Raised-sine S-bend geometry used for waveguide routing.

Figure 2.8: Final geometrical elements adopted for the OPA platform. (a) cross section of the Ge-on-Si waveguide with air cladding and silicon substrate. (b) raised-sine S-bend used to route the waveguides between the splitting stages while minimizing radiation losses.

Chapter 3

Optical Power Splitting Network

Once the material platform and reference waveguide geometry have been defined, the next step in the design of the optical phased array concerns the distribution of optical power among the radiating elements. The splitting stage plays a crucial role in determining the uniformity of excitation across the array, directly affecting the overall radiation pattern and achievable beam quality.

In an integrated OPA, the optical signal must be progressively divided into multiple branches while preserving power balance, minimizing excess losses, and maintaining phase consistency. These requirements become increasingly critical as the number of emitters grows, since power imbalance and insertion losses accumulate along cascaded structures.

In this chapter, two alternative 1x2 splitting solutions are investigated: an adiabatic Y-branch and a multimode interference (MMI) splitter. Both devices are initially designed at the central wavelength of 6 μm, corresponding to the midpoint of the $4-8$ μm operating band. Their performance is then evaluated across the full spectral range in order to assess broadband robustness and determine the most suitable architecture for a cascaded 16-emitter configuration.

3.1 Role of the Power Splitting Stage in Optical Phased Arrays

In an integrated optical phased array (OPA), the power splitting stage is responsible for distributing the optical signal from a single input waveguide to multiple radiating elements. This process must be performed while preserving amplitude uniformity, limiting excess losses, and maintaining phase coherence throughout the array. These requirements are fundamental for achieving high beam quality and suppressing undesired sidelobes in the far-field radiation pattern [3, 4].

The far-field response of an OPA can be interpreted as the product of the element radiation pattern and the array factor, which depends on the relative amplitude and phase of each emitter. While phase control determines the steering angle of the beam, the amplitude distribution directly influences sidelobe levels and overall radiation efficiency. Ideally, each emitter should be excited with equal power in order to maximize the main lobe intensity and ensure predictable beamforming behavior. Any imbalance introduced

during the splitting process propagates through the array and may degrade performance [5].

In practical integrated implementations, power distribution is achieved through cascaded splitting structures. As the number of emitters increases, insertion losses accumulate along the splitting tree, potentially limiting the optical power available at the output. For large-scale arrays, this aspect becomes critical since excessive losses reduce the achievable optical efficiency and may require higher input power levels [4].

Therefore, the design of the splitting network must satisfy three main criteria: balanced power division, low excess loss, and robustness over the operating wavelength range. In the present work, these aspects are evaluated for two alternative 1x2 splitter configurations, which constitute the fundamental building block of the cascaded architecture adopted for the 16-emitter array.

3.2 Y-Branch Splitter: Design and Performance at 6 µm

The Y-branch splitter is the first architecture considered for power division within the OPA feeding network. Its operating principle is based on an adiabatic transition in which the fundamental guided mode gradually evolves into two separate modes propagating in distinct output arms. If the branching region is sufficiently smooth, the input mode is progressively redistributed without exciting higher-order modes, ideally resulting in an equal power split.

The initial geometry is derived from the reference configuration presented in [11] and is adapted to the Ge-on-Si strip waveguide platform defined in Chapter 2. The design is carried out at the central wavelength of 6 µm, and the analysis focuses on the fundamental mode (mode 0), consistent with the waveguide study previously performed.

A parametric optimization is conducted in RSoft in order to obtain a balanced power division between the two output arms. The parameters included in the optimization process are: (i) the separation between the output waveguides, (ii) the length of the branching arms, and (iii) the length of the input taper section.

Although the taper section is included among the design variables, numerical tests indicate that it has a limited impact on the final power distribution, while arm length and output separation play a more significant role. The optimized geometric parameters are summarized in Table 3.1.

Table 3.1: Optimized geometrical parameters of the Y-branch splitter at 6 µm.

Parameter	Value [µm]
Output waveguide separation	15.86
Branching arm length	58.43
Input taper length	142.9

The simulations with the beam propagation method are then performed at a wavelength of 6 µm in order to verify the field evolution along the device. The simulated field distribution and the power monitored at the output ports are reported in Fig. 3.1.

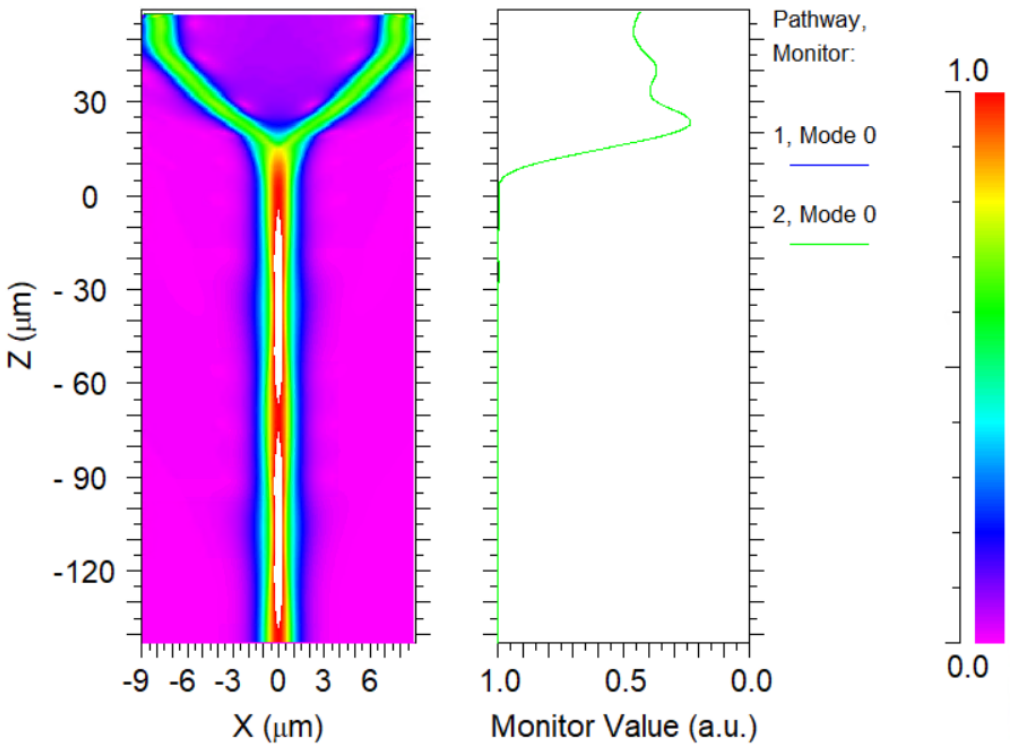

Figure 3.1: BeamPROP simulation of the optimized Y-branch splitter at 6 µm for mode 0. Left: optical field propagation along the device, showing the adiabatic transition from a single input mode to two separated output modes. Right: monitored output power in the two branches, indicating an approximately balanced power division with small excess losses.

The simulation confirms that, at the design wavelength of 6 µm, the optical power is evenly distributed between the two output arms. The monitored signals show that both branches carry approximately the same fraction of the input power, indicating a symmetric splitting behavior. However, the output power in each arm is slightly lower than the ideal value of $0.5\,P_{\text{in}}$, revealing the presence of excess losses introduced in the branching region. These losses are attributed to non-ideal adiabatic transitions and weak radiation effects occurring during mode separation.

A quantitative evaluation of insertion losses over the entire $4-8$ µm wavelength range is presented in Sec.3.4, where this architecture is compared with the MMI-based solution.

3.3 MMI 1x2 Splitter: Design and Performance at 6 µm

As an alternative to the adiabatic Y-branch, a multimode interference (MMI) splitter is investigated. Unlike the Y-branch, the MMI operates based on the self-imaging principle: when an input field excites multiple guided modes in a multimode section, constructive interference at specific propagation lengths recreates one or more replicas of the input

field profile. By properly choosing the width and length of the multimode region, a controlled 1×2 power division can be achieved.

The initial geometry is derived from the same reference configuration described in [11] and adapted to the Ge-on-Si strip waveguide platform introduced in Chapter 2. The design is performed at 6 µm and the analysis focuses on the fundamental mode (mode 0), ensuring consistency with the waveguide and Y-branch studies.

A parametric optimization is carried out in RSoft in order to achieve balanced power splitting at the output ports. The parameters included in the optimization are: (i) the length of the input and output tapers (assumed identical), (ii) the separation between the output waveguides, (iii) the length of the multimode section, and (iv) the width of the multimode region.

The optimized geometric parameters are summarized in Table 3.2.

Table 3.2: Optimized geometrical parameters of the 1×2 MMI splitter at 6 µm.

Parameter	Value [µm]
MMI width	9.43
MMI length	32.97
Input/Output taper length	28.76
Output waveguide separation	4.9

Beam propagation simulations are performed at 6 µm to verify the field evolution inside the multimode region and the power distribution at the output ports. The corresponding simulation results are shown in Fig. 3.2.

The simulation confirms that the optical power is symmetrically distributed between the two output ports at the design wavelength. Both branches receive approximately half of the input power, indicating correct self-imaging behavior within the multimode section. Unlike the case of the Y-branch, the monitored output signals show that the total transmitted power remains very close to the input power, suggesting negligible excess losses at 6 µm. This result highlights the intrinsic robustness of the self-imaging mechanism at the design wavelength.

A quantitative comparison between the Y-branch and MMI architectures over the entire $4-8$ µm wavelength range is presented in Sec.3.4, where the most suitable solution for the OPA feeding network is selected.

3.4 Broadband Analysis in the 4-8 µm Range and Device Selection

In order to evaluate the robustness of the two splitting architectures, a broadband analysis is performed in the $3-9$ µm wavelength range, with a particular focus on the operational interval between 4 µm and 8 µm. The insertion loss is computed as

$$\text{Loss (dB)} = 10 \log_{10} \left(\frac{P_{\text{in}}}{P_{\text{out}}} \right), \tag{3.1}$$

The results for both devices are reported in Fig. 3.3.

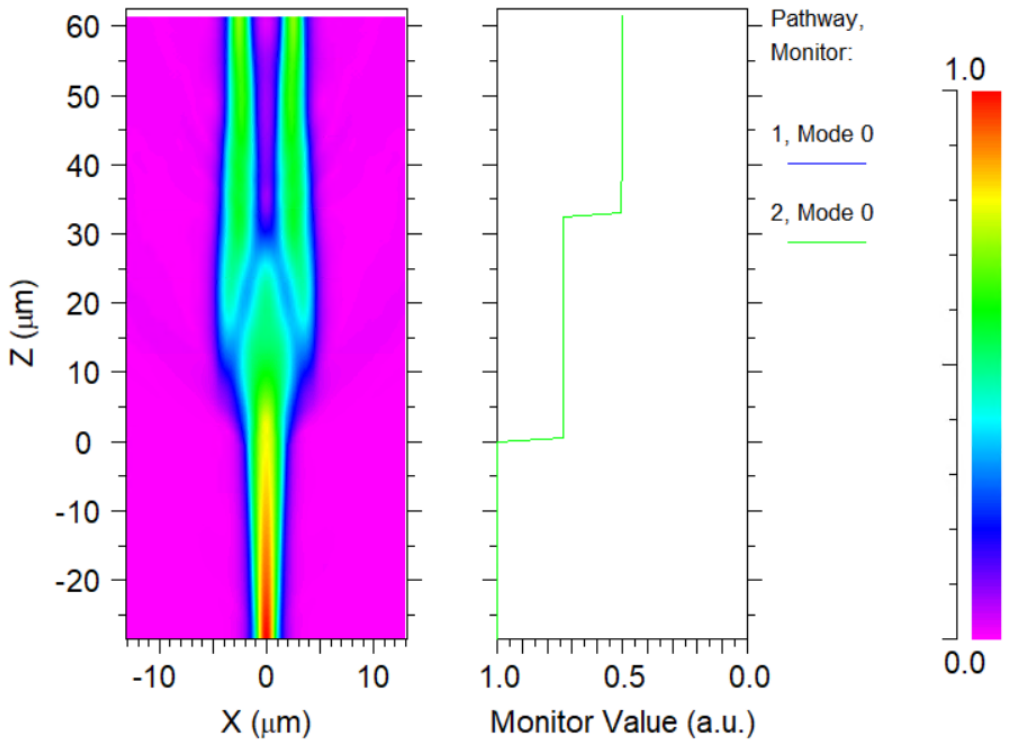

Figure 3.2: BeamPROP simulation of the optimized 1×2 MMI splitter at 6 µm for mode 0. Left: optical field propagation inside the multimode section, illustrating the self-imaging mechanism. Right: monitored output power in the two branches, showing an approximately balanced division with negligible excess losses.

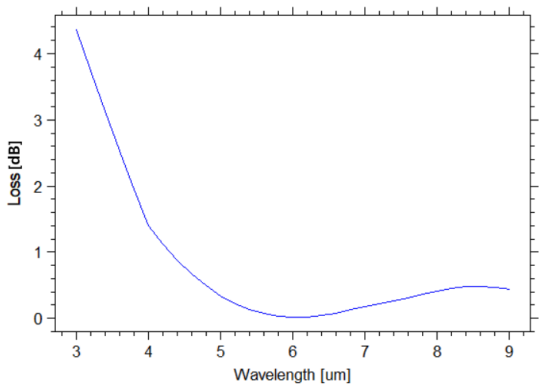

(a) Insertion loss of the 1×2 MMI splitter as a function of wavelength.

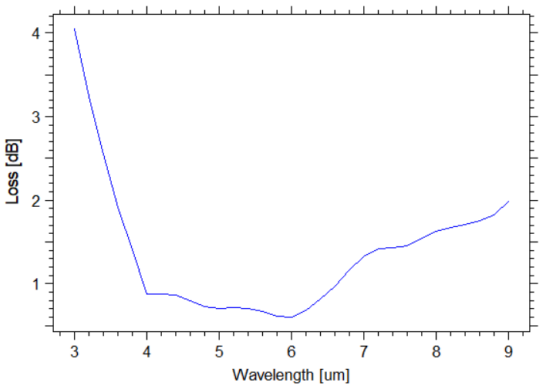

(b) Insertion loss of the Y-branch splitter as a function of wavelength.

Figure 3.3: Broadband insertion loss comparison between the optimized MMI and Y-branch splitters over the $3-9$ µm wavelength range. The operational interval of interest ($4-8$ µm) is highlighted in the analysis.

At the design wavelength of 6 µm, the MMI splitter exhibits an insertion loss of approximately 0.016 dB, while the Y-branch shows a significantly higher loss of about 0.59 dB. This confirms that the MMI is strongly optimized at the central wavelength and benefits from an efficient self-imaging mechanism.

Moving away from 6 µm, both architectures exhibit increased losses, as expected due to the wavelength dependence of modal interference and adiabatic transitions. At 4 µm, the Y-branch shows a lower insertion loss (approximately 0.88 dB) compared to the MMI (approximately 1.39 dB). In contrast, at 8 µm the MMI performs better, with a loss of approximately 0.41 dB compared to 1.86 dB for the Y-branch.

Overall, while neither architecture maintains perfectly constant performance over the entire spectral range, the MMI splitter demonstrates superior behavior at the design wavelength and competitive performance over most of the $4-8$ µm interval. In addition, the significantly lower insertion loss at 6 µm makes the MMI particularly attractive for a system optimized around this central wavelength.

Based on this analysis, the MMI architecture is selected as the reference splitting element for the OPA feeding network. The next section describes the implementation of a cascaded MMI structure to generate the required number of output channels.

3.5 Cascaded Splitting Architecture for a 16-Emitter Array

In order to feed a 16-emitter OPA, the selected 1×2 MMI splitter is replicated in a balanced binary-tree configuration, resulting in four cascading stages (1→2→4→8→16). Routing between consecutive stages is implemented through raised-sine S-bends, whose vertical length is chosen according to the required horizontal displacement to minimize additional bending losses. All simulations are performed at the design wavelength of 6 µm, consistent with the optimization of the component-level discussion outlined in the previous sections.

A BeamPROP simulation of the complete splitting network is reported in Fig. 3.4. The field evolution confirms the progressive power distribution through the four stages up to the 16 output waveguides.

To provide a quantitative assessment, the output power at each channel is extracted through dedicated monitors and summarized in the bar plot shown in Fig. 3.5.

The cumulative insertion loss of the splitting network is evaluated from the total transmitted power

$$P_{\text{tot,out}} = \sum_{i=1}^{16} P_i \tag{3.2}$$

and is expressed in dB as

$$\text{Loss}_{\text{net}} = -10 \log_{10} \left(\frac{P_{\text{tot,out}}}{P_{\text{in}}} \right) \tag{3.3}$$

With $P_{\text{in}} = 1$, the simulated network exhibits an overall insertion loss of $\text{Loss}_{\text{net}} = 2.418$ at 6 µm. This confirms that the cascaded MMI architecture remains compatible with a scalable OPA implementation while preserving low-loss operation at the central wavelength.

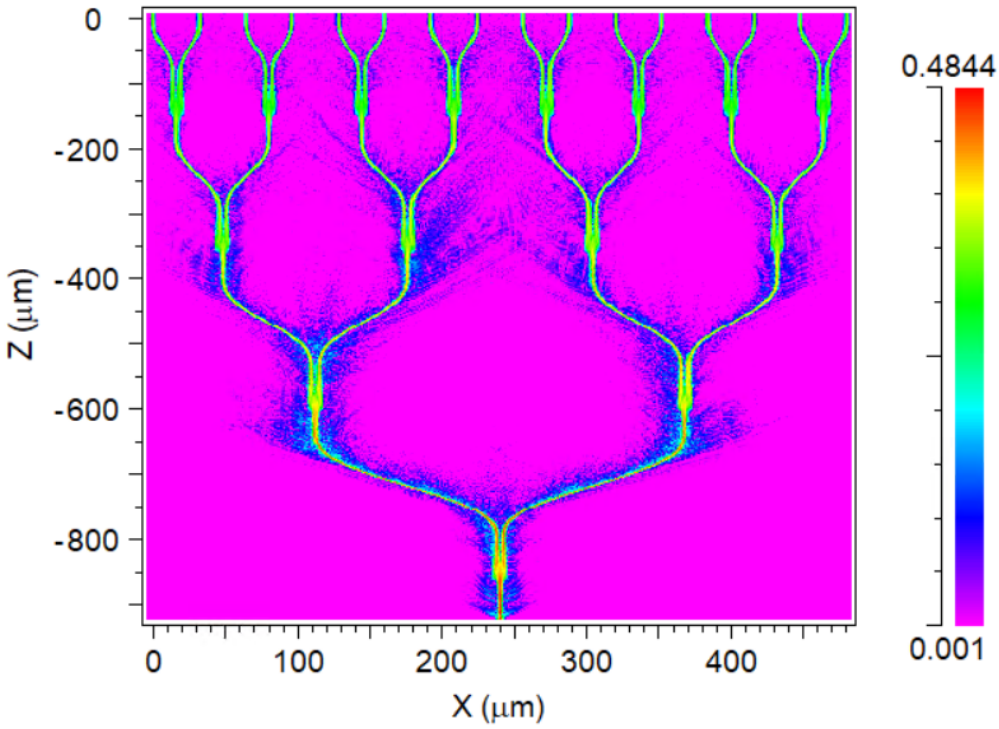

Figure 3.4: BeamPROP simulation of the cascaded MMI splitting network (1→2→4→8→16) at 6 µm for mode 0. The field evolution shows progressive power division across the four stages up to the 16 output waveguides.

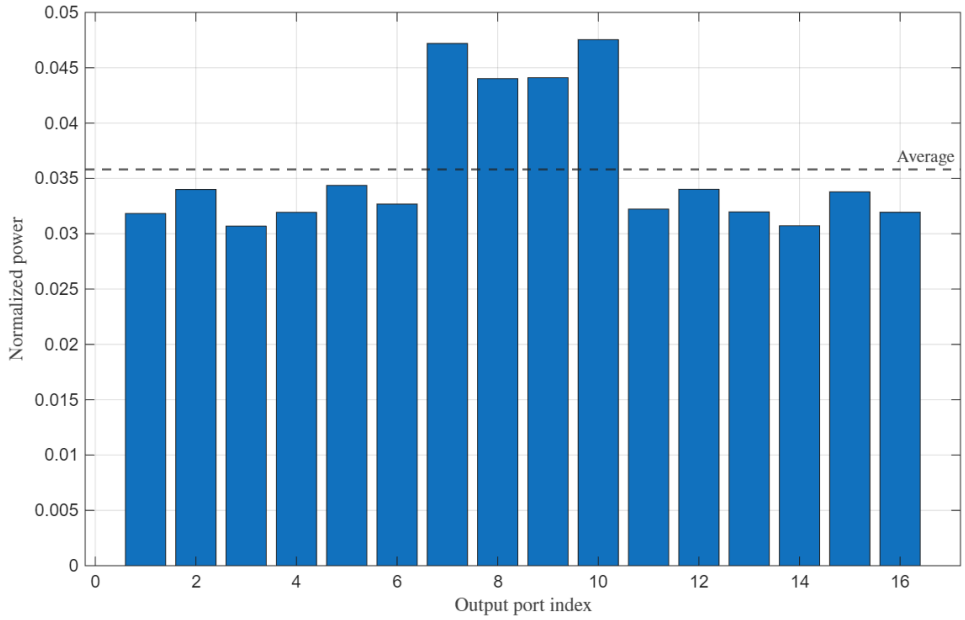

Figure 3.5: Normalized output power at the 16 ports of the cascaded MMI splitting network at 6 µm ($P_{\text{in}} = 1$).

Chapter 4

Thermo-Optic Phase Shifter Design

Controlling the optical phase of each emitter is a fundamental requirement for beam steering in optical phased arrays. In the mid-infrared range, the thermo-optic effect represents a practical and technologically mature mechanism to locally tune the effective refractive index of a waveguide. By inducing a controlled temperature variation in the guiding region, it is possible to modify the propagation constant and, consequently, the accumulated optical phase.

In this chapter, the thermo-optic modulation of the previously defined Ge-on-Si waveguide is investigated. The analysis follows a progressive approach. First, the dependence of the effective index on temperature is evaluated in order to quantify the achievable index variation. Based on this result, an effective thermo-optic coefficient is extracted for the guided mode. The required phase shift is then translated into a target interaction length. Finally, thermal simulations are carried out to assess the power requirements and to define the final heater geometry, taking into account practical trade-offs between efficiency, footprint, and thermal isolation.

4.1 Phase Shifting Mechanisms for Optical Phased Arrays

The ability to independently control the optical phase of each emitting channel is the key enabler of beam steering in optical phased arrays. By introducing a controlled phase difference between adjacent emitters, the far-field interference pattern can be reshaped and steered without any mechanical movement. For this reason, the phase-shifting mechanism represents one of the most critical building blocks of the overall system.

Several approaches have been proposed in the literature to implement phase control in integrated photonic platforms. In silicon-based OPAs, carrier injection and carrier depletion techniques are widely adopted, exploiting the plasma dispersion effect to locally modify the refractive index. These solutions enable relatively fast modulation speeds and are often compatible with CMOS processes. However, they require complex doping profiles and electrical isolation strategies, and they typically introduce additional optical losses due to free-carrier absorption. For large-scale arrays, cumulative loss and power

dissipation can become limiting factors [3].

Electro-optic phase shifting represents another possible solution, particularly in materials exhibiting a strong Pockels effect. While this approach can provide high-speed modulation with limited static power consumption, it relies on material platforms that are not always compatible with standard Ge-on-Si integration or mid-infrared operation. Moreover, in the wavelength range considered in this work, material choices offering a strong linear electro-optic response are limited. Micro-electromechanical (MEMS) approaches have also been explored, where the optical path length is modified by physically displacing waveguide sections or gratings.

Although such techniques can achieve large phase shifts with low optical loss, they reintroduce mechanical complexity and are generally less attractive when compactness and robustness are primary design targets. In contrast, thermo-optic phase shifting relies on the intrinsic temperature dependence of the refractive index. By locally heating the waveguide core, the effective index of the guided mode is modified, leading to a controllable variation of the accumulated optical phase. This mechanism has been extensively used in integrated photonics due to its structural simplicity and fabrication compatibility. While its modulation speed is inherently limited by thermal time constants, the approach is particularly suitable for beam steering applications, where switching speeds are typically much lower than in data modulation systems [5].

In the mid-infrared range, and especially in a Ge-on-Si platform, the thermo-optic effect offers additional practical advantages. The required heater structures can be implemented without modifying the optical core geometry, and the absence of intentional doping preserves low propagation losses in the passive waveguides. Given that the primary objective of this work is to demonstrate a scalable and low-loss OPA architecture rather than ultra-fast modulation, thermo-optic tuning represents a well-balanced solution between design complexity, optical performance, and fabrication feasibility. For these reasons, the thermo-optic approach is selected in this work as the reference phase-shifting mechanism. The following sections quantify its impact on the effective index of the Ge-on-Si waveguide and translate the resulting index variation into a practical heater design.

4.2 Temperature Dependence of the Effective Index

Once the thermo-optic mechanism has been selected as the phase control strategy, the first step consists of quantifying how the guided mode responds to temperature variations. The phase shift accumulated along a waveguide section depends directly on the effective index of the propagating mode, which, in turn, is influenced by the temperature-dependent refractive indices of the materials involved. In a first-order approximation, the real part of the refractive index can be expressed as a linear function of temperature

$$n(T) = n(T_0) + \left(\frac{\mathrm{d}n}{\mathrm{d}T}\right)\Delta T \tag{4.1}$$

where $\Delta T = T - T_0$. In this work, the thermo-optic coefficients are assumed to be $(\mathrm{d}n/\mathrm{d}T)_{\mathrm{Ge}} = 1 \times 10^{-4}\,\mathrm{K}^{-1}$ for germanium and $(\mathrm{d}n/\mathrm{d}T)_{\mathrm{Si}} = 2.4 \times 10^{-4}\,\mathrm{K}^{-1}$ for silicon. Both contributions are considered since the Ge core is not thermally isolated from

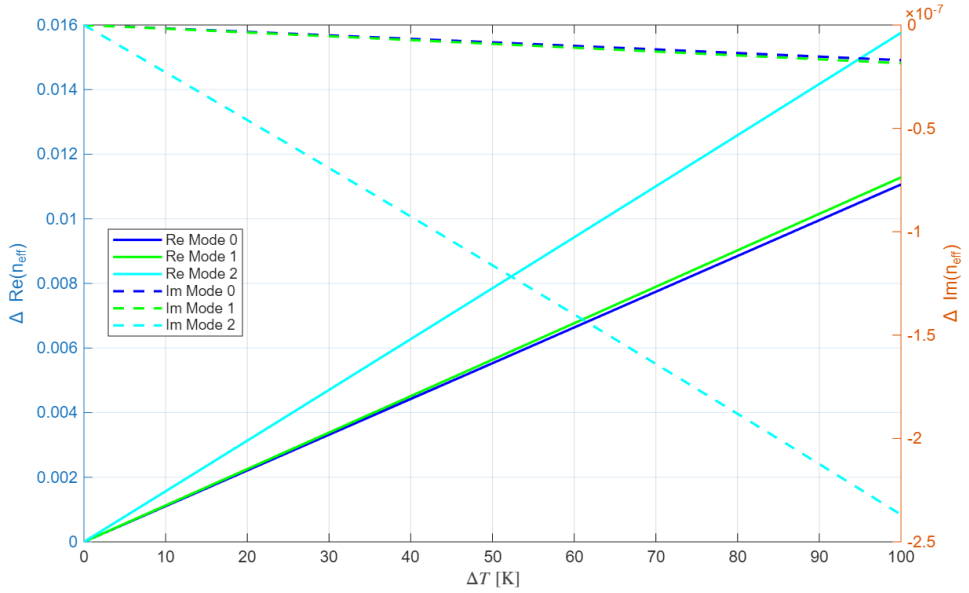

Figure 4.1: Variation of the effective index as a function of temperature increase ΔT at 6 µm. The plot shows $\Delta n_{\text{eff}}(\Delta T) = n_{\text{eff}}(\Delta T) - n_{\text{eff}}(0)$ for the first three guided modes, highlighting a nearly linear dependence over $\Delta T \in [0{,}100]$ K.

the substrate. As will be shown in the thermal analysis, the silicon region beneath the waveguide experiences a comparable temperature increase, and therefore its refractive index variation affects the modal confinement and propagation constant. To evaluate the overall impact on propagation, the effective index is computed as a function of temperature increase for the first three guided modes of the reference waveguide geometry at 6 µm. Rather than reporting the absolute value of n_{eff}, the variation

$$\Delta n_{\text{eff}}(\Delta T) = n_{\text{eff}}(\Delta T) - n_{\text{eff}}(0) \tag{4.2}$$

is analyzed over the range $\Delta T \in [0{,}100]$ K. The corresponding curves are shown in Fig. 4.1.

Within the investigated interval, the dependence of Δn_{eff} on temperature is found to be nearly linear. This behavior indicates that, for moderate temperature excursions, the phase response of the waveguide can be accurately approximated by a constant effective thermo-optic coefficient. At the same time, slight differences in slope are observed among the first three modes, reflecting their different spatial overlap with the germanium core and the silicon substrate. The linear relationship between the temperature increase and the effective index variation establishes the fundamental link between thermal actuation and optical phase control. In the next section, this dependence is translated into a required interaction length to achieve a target phase shift.

The thermo-optic analysis presented above accounts for the temperature dependence of both germanium and silicon. However, the optical simulations performed in RSoft do not allow the definition of multilayer structures including substrates with different effective indices. In order to reproduce the temperature dependence observed in the

full waveguide analysis, an effective thermo-optic coefficient is therefore introduced for the germanium material. The value of $(\mathrm{d}n/\mathrm{d}T)_{\mathrm{Ge,eff}}$ is chosen so that the resulting variation of the effective index matches the dependence $\Delta n_{\mathrm{eff}}(\Delta T)$ obtained from the waveguide simulations. In particular, the effective coefficient is calibrated to reproduce the slope dn_{eff}/dT of the fundamental mode. With this approach, the resulting effective-index variation closely follows the reference curve, with discrepancies limited to the sixth decimal digit for small temperature increments. This simplified model allows the thermo-optic phase shift to be accurately captured in the optical simulations while maintaining a manageable numerical complexity.

4.3 Phase Shift Requirement and Heater Length Estimation

The phase variation induced by a temperature increase can be translated into a required interaction length for phase tuning. For a guided mode propagating over a length L, a perturbation of the effective index Δn_{eff} produces a phase shift

$$\Delta\phi = \frac{2\pi}{\lambda}\,\Delta n_{\mathrm{eff}}\,L \tag{4.3}$$

By imposing a target phase shift of $\Delta\phi = \pi$, the interaction length required to achieve a 2π-shift is

$$L_\pi = \frac{\lambda}{\Delta n_{\mathrm{eff}}} \tag{4.4}$$

Using the dependence $\Delta n_{\mathrm{eff}}(\Delta T)$ obtained for mode 0 at $\lambda = 6$ µm, L_π is evaluated for temperature increases up to 100 K. The resulting curve is shown in Fig. 4.2 and confirms the expected inverse relationship between $L_{2\pi}$ and ΔT.

For reference, a temperature increase of $\Delta T = 20$ K corresponds to $\Delta n_{\mathrm{eff}} \approx 2.2\times10^{-3}$ and requires $L_{2\pi} \approx 2.71$ mm. Increasing the temperature rise to $\Delta T = 50$ K leads to $\Delta n_{\mathrm{eff}} \approx 5.5\times10^{-3}$ and reduces the required length to $L_{2\pi} \approx 1.08$ mm. Finally, for $\Delta T = 100$ K, $\Delta n_{\mathrm{eff}} \approx 1.11\times10^{-2}$ and the interaction length decreases to $L_{2\pi} \approx 542$ µm.

These values provide a practical reference for design. While larger temperature variations enable shorter phase shifters, they may also increase power consumption and thermal cross-talk. The final heater design, therefore, results from a trade-off between the achievable temperature rise, footprint, and power efficiency.

4.4 Thermal Simulation and Power Analysis

The phase-shifter design requires translating the optical phase target into a realistic thermal actuation level. Based on the $L_\pi(\Delta T)$ analysis presented in the previous section, a reference temperature increase of $\Delta T_{\mathrm{Ge}} = 54$ K is selected. For mode 0 at $\lambda = 6$ µm, this corresponds to an interaction length of $L_{2\pi} = 1004.18$ µm.

This operating point is chosen as a compromise between compactness and thermal load. Selecting a moderate temperature rise keeps the interaction length below one

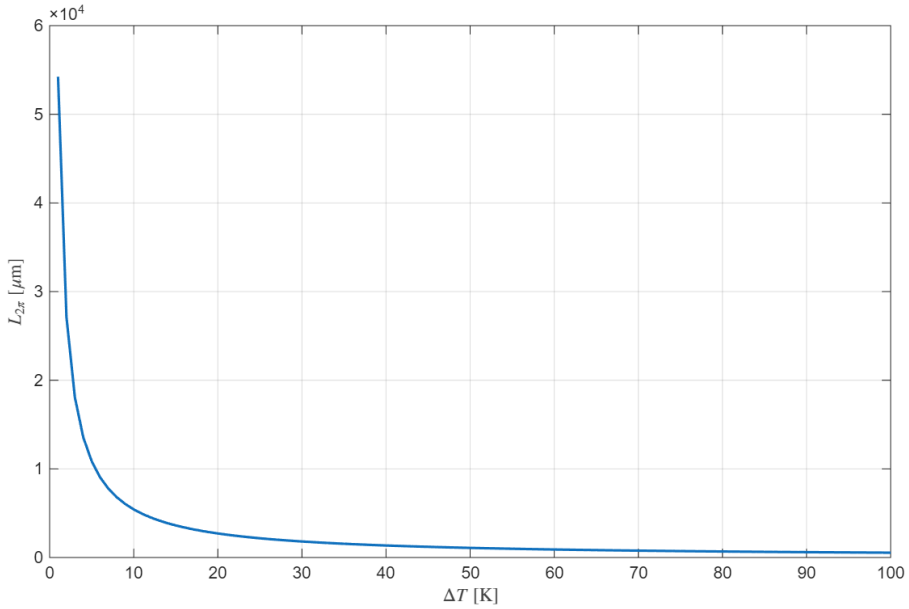

Figure 4.2: Required interaction length L_π to achieve a π phase shift at $\lambda = 6$ µm as a function of temperature increase ΔT for mode 0.

millimeter, which simplifies both the optical simulation domain and the overall device footprint. At the same time, the chosen temperature increase remains within a range compatible with thermo-optic actuation in integrated photonic platforms. Should power consumption or thermal management constraints require it, the interaction length could be adjusted according to the $L_{2\pi}(\Delta T)$ relationship discussed above.

The heater geometry is derived from the thermo-optic phase-shifter layout reported in [9], which is reproduced and adapted here to the Ge-on-Si platform considered in this thesis. A lateral titanium heater is placed at a distance of 3 µm from the waveguide core. The heater has a rectangular cross-section of 0.15 µm×6 µm and air is assumed to be the upper cladding. The structure includes isolation trenches positioned around the waveguide region, as illustrated in Fig. 4.3. These trenches are introduced to improve thermal confinement and reduce the spread of lateral heat into the substrate.

Thermal simulations are performed in COMSOL on a single waveguide section, including the Ge core, the silicon substrate, the air cladding, and the titanium heater. The objective of the simulation is to determine the power required to achieve a temperature increase of $\Delta T_{\mathrm{Ge}} = 54$ K in the germanium guiding region.

Two configurations are analyzed: with and without trenches. In both cases, the actuation level is adjusted so that the temperature rise in the Ge core reaches the same target value. This approach allows for a physically consistent comparison in terms of efficiency since the required phase shift depends on ΔT_{Ge} rather than directly on electrical power.

The resulting temperature distributions are reported in Fig. 4.4. When trenches are included, the heat remains more localized around the waveguide core, leading to a steeper temperature gradient and reduced thermal diffusion into the surrounding silicon.

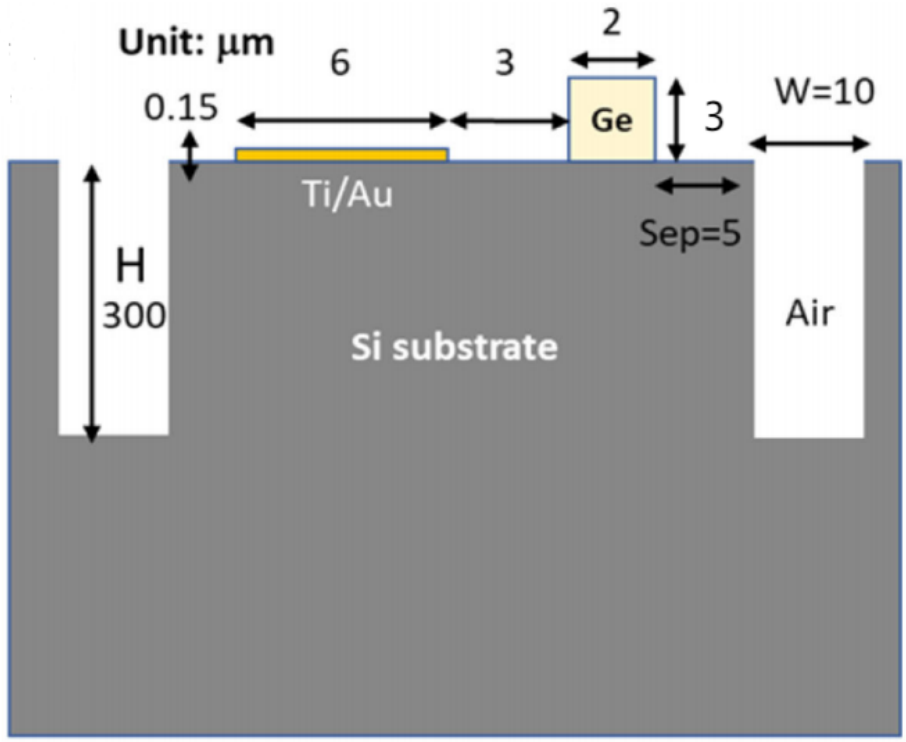

Figure 4.3: Thermo-optic phase shifter geometry adapted from [9]. The structure includes a lateral titanium heater, air upper cladding, and isolation trenches to improve thermal confinement.

As a consequence, the same ΔT_{Ge} can be achieved with a lower heater temperature and reduced power dissipation.

The comparison between the two configurations highlights the impact of thermal isolation. In both cases, the electrical bias is fixed at 3 V and the actuation is adjusted to reach a temperature increase of $\Delta T_{\mathrm{Ge}} = 54$ K in the guiding region.

When trenches are included, a current density of approximately 4.02×10^{10} A/m^2 is required, resulting in an increase of the heater temperature of approximately 56 K. In the absence of trenches, achieving the same temperature rise in the germanium core requires a significantly higher current density of 1.199×10^{11} A/m^2, leading to a heater temperature increase of approximately 70 K.

Since the applied voltage is the same in both simulations, the dissipated power scales proportionally with the current density. In the trench-assisted configuration, the electrical power required to achieve $\Delta T_{\mathrm{Ge}} = 54$ K is approximately 108 mW. In contrast, without trenches, the same temperature increase requires about 324 mW.

This significant difference demonstrates the effectiveness of thermal isolation: the inclusion of trenches reduces the required actuation power by more than a factor of two while simultaneously lowering the heater temperature. The improvement in thermal confinement confirms that trenches play a crucial role in enhancing the efficiency of the

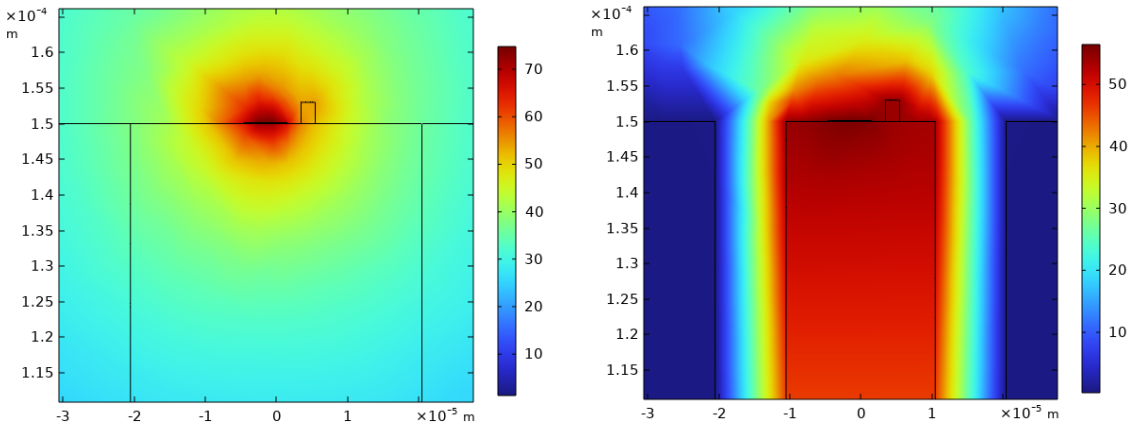

(a) Without trenches.

(b) With trenches.

Figure 4.4: Temperature distribution obtained from COMSOL simulations for a target $\Delta T_{\mathrm{Ge}} = 54$ K. Isolation trenches improve thermal confinement and reduce the power required to achieve the same temperature increase in the guiding region.

thermo-optic phase shifter.

An additional aspect of interest is thermal cross-talk toward neighboring channels. From the trench-assisted simulation, the silicon region laterally adjacent to the trenches experiences only a limited temperature rise of approximately 0.5 K. This result suggests that the thermal perturbation is largely confined within the phase-shifter region, supporting the suitability of the selected geometry for dense arrays where multiple heaters operate in proximity.

The temperature maps further show that the silicon substrate beneath the germanium core experiences a temperature increase comparable to that of the guiding region. This observation justifies the modeling approach adopted in Sec. 4.2, where the thermo-optic contribution of silicon was explicitly included in the evaluation of Δn_{eff}.

4.5 Final Heater Geometry and Design Trade-Off

Based on the analysis presented in this chapter, the thermo-optic phase shifter adopted in this work is designed to provide a full 2π phase tuning range. Using the temperature dependence extracted in Sec.4.2, a temperature increase of $\Delta T_{\mathrm{Ge}} = 54$ K corresponds to a 2π phase shift over an interaction length of approximately 1004.18 µm at $\lambda = 6$ µm.

The heater geometry follows the configuration introduced earlier in this chapter: a lateral titanium heater placed 3 µm from the waveguide core, with a cross-section of 0.15 µm×6 µm and air as the upper cladding. Thermal isolation trenches are included in the final layout, as they significantly improve thermal confinement and reduce the electrical power required to reach the target temperature increase.

It is important to note that the geometry adopted here should not be regarded as a universal solution. The design of thermo-optic phase shifters strongly depends on fabrication constraints and system-level considerations. For instance, the pitch between

adjacent waveguides may be determined by the electrical routing strategy used to contact the heaters. If techniques such as wire bonding are employed, as in [9], additional space may be required to accommodate contact pads. This can lead to a larger waveguide spacing in the phase-shifter region.

A larger pitch, in turn, affects the routing sections connecting the splitter network to the heated waveguides. In particular, longer S-bend transitions may be required to gradually separate the waveguides and avoid excessive bending losses. Similarly, the heated length and the increase in operating temperature can be adjusted depending on the specific application requirements. Designs favoring lower power consumption may employ longer heaters operating at smaller temperature variations, while compact implementations may accept higher thermal loads in exchange for a reduced device footprint.

For these reasons, the parameters adopted in this work should be interpreted as a representative design point rather than a fixed rule. The methodology developed in the previous sections provides the necessary framework to adapt the phase-shifter geometry to different technological constraints and system requirements.

The geometry adopted for the thermo-optic phase shifter is illustrated in Fig. 4.5, showing the relative positioning of the titanium heater, the germanium waveguide, and the thermal isolation trenches.

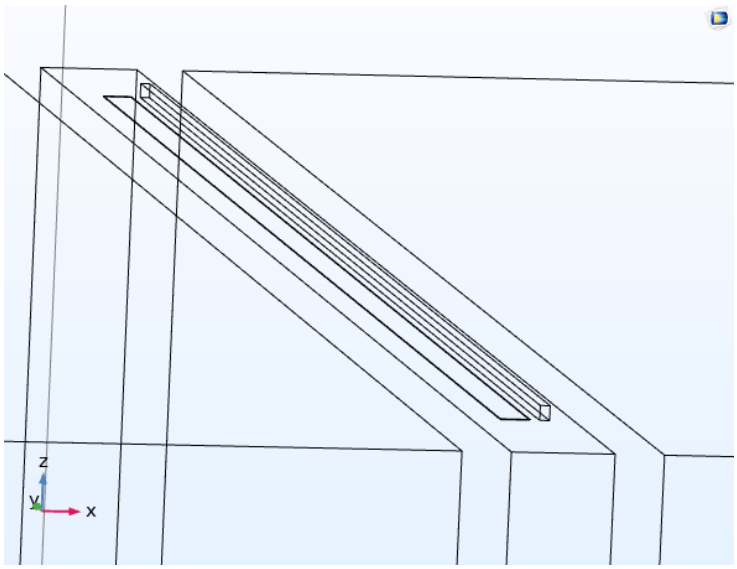

Figure 4.5: Three-dimensional view of the thermo-optic phase shifter geometry used in this work. The titanium heater is positioned beside the germanium waveguide at a distance of 3 μm, while thermal isolation trenches are introduced in the silicon substrate to improve heat confinement around the waveguide region.

Chapter 5

Emitter Design and Far-Field Analysis

The previous chapters focused on the design of the main building blocks required to distribute and control the optical signal inside the optical phased array. In particular, the waveguide platform was defined, the optical power splitting network was designed, and thermo-optic phase shifters were introduced to enable independent phase control of each channel. These elements together allow the optical field to be routed and phase-modulated across the array.

The final step in the realization of the optical phased array consists in converting the guided optical signals into radiated fields and analyzing the resulting far-field pattern. This process is determined both by the characteristics of the emitting elements and by the relative phase distribution among the different channels of the array. As a consequence, the design of the emitters and the analysis of the output radiation pattern play a central role in determining the overall performance of the device.

This chapter therefore addresses the emission stage of the optical phased array and the resulting far-field response. First, the physical principles governing the formation of the far-field pattern in optical phased arrays are discussed, with particular attention to the differences between one-dimensional and two-dimensional configurations. The design of the emitter adopted in this work is then presented. Subsequently, calibration strategies for optical phased arrays are briefly reviewed, highlighting their importance in practical implementations. Finally, the far-field response of the designed array is analyzed in order to evaluate the beam profile generated by the device.

5.1 Far-Field Formation in Optical Phased Arrays

In an OPA, the radiation pattern observed in the far field is generated by the coherent superposition of the optical fields emitted by multiple radiating elements. Each emitter converts the guided optical mode propagating in the waveguide into radiation directed toward free space. When several emitters operate simultaneously, the resulting field distribution is determined by the interference of the contributions generated by all the elements of the array.

The radiation pattern of an optical phased array can be conveniently interpreted as the product of two contributions: the radiation profile of the individual emitter and the interference pattern generated by the spatial distribution of the emitters. This relationship can be written as

$$E(\theta) = E_{\text{elem}}(\theta)\, AF(\theta) \tag{5.1}$$

where $E_{\text{elem}}(\theta)$ represents the radiation pattern of a single emitter, often referred to as the *element factor*, while $AF(\theta)$ denotes the *array factor*, which describes the interference between the fields emitted by the different elements of the array [3, 5].

The element factor depends on the geometry and radiation mechanism of the emitter and determines the angular envelope of the emitted beam. In integrated OPAs, this term is mainly influenced by the design of the radiating structure, which is responsible for coupling the optical field from the waveguide into free space.

The array factor depends only on the spatial distribution and the relative phase of the emitters. Considering a linear array composed of N elements equally spaced by a distance d, the array factor can be written as

$$AF(\theta) = \sum_{n=0}^{N-1} A_n e^{j(\phi_n + knd\sin\theta)} \tag{5.2}$$

where A_n and ϕ_n represent the amplitude and phase associated with the n-th emitter, $k = 2\pi/\lambda$ is the optical wavenumber and θ is the observation angle.

The intensity distribution of the radiated beam is obtained from the square modulus of the electric field

$$I(\theta) = |E(\theta)|^2. \tag{5.3}$$

One of the main advantages of optical phased arrays is the possibility of steering the emitted beam without the use of mechanical components. This is achieved by introducing a controlled phase difference between adjacent emitters. If the phase applied to the n-th emitter is expressed as

$$\phi_n = n\Delta\phi, \tag{5.4}$$

the condition for constructive interference determines the direction of the main beam. In this case, the steering angle θ_0 satisfies

$$kd\sin\theta_0 + \Delta\phi = 0. \tag{5.5}$$

This relation shows that the emission angle can be tuned by modifying the phase difference $\Delta\phi$ between adjacent channels, which, in integrated OPAs, is typically controlled through thermo-optic or electro-optic phase shifters.

Another parameter that strongly influences the far-field response is the spacing between emitters. If the pitch d becomes comparable to or larger than the optical wavelength, additional maxima known as *grating lobes* may appear in the radiation pattern.

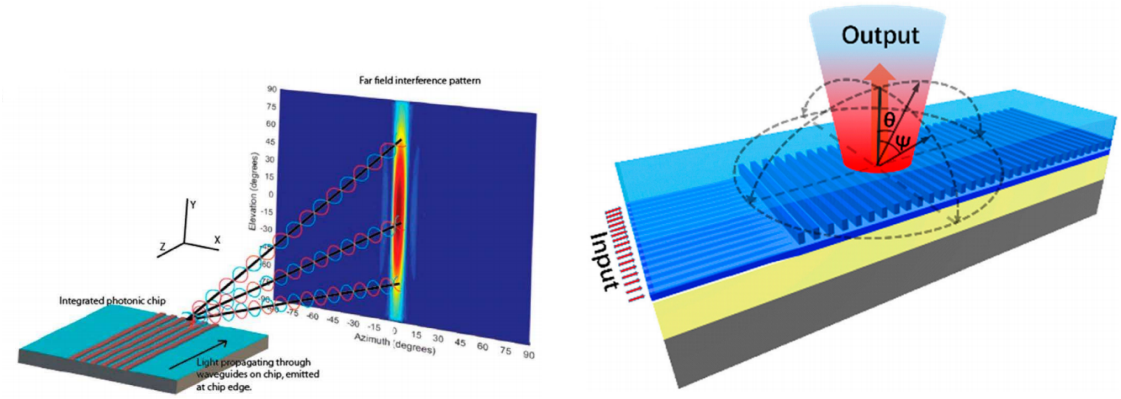

(a) 1D radiation.

(b) 2D radiation.

Figure 5.1: Conceptual representation of one-dimensional and two-dimensional radiation in optical phased arrays. In the 1D case the beam is steered along a single angular coordinate, in the 2D case the radiation pattern extends over two angular directions.

For this reason, the spacing between emitters is usually kept as small as allowed by the technological constraints of the platform.

The dimensionality of the radiation pattern depends both on the array configuration and the emission properties of the radiating elements. In many integrated implementations, the emitters are arranged along a linear array, allowing the beam to be steered along a single angular coordinate. In this case, the radiation pattern forms a narrow beam in the steering direction, while the angular distribution in the orthogonal direction is mainly determined by the radiation profile of the individual emitters.

Alternatively, emitter structures can be designed to distribute the radiated optical power over two angular directions, enabling a two-dimensional radiation pattern. In this case, the far-field distribution can be controlled along both angular coordinates, allowing beam steering over a two-dimensional field of view. While such solutions offer greater flexibility in beam control, they generally require more complex emitter designs and more demanding phase control across the array.

For these reasons, many integrated OPA implementations adopt one-dimensional steering architecture combined with emitters engineered to produce the desired radiation profile in the orthogonal direction [3, 5]. This approach simplifies the photonic layout while still enabling effective beam steering for applications such as optical sensing and ranging systems.

5.2 Design of the One-Dimensional Emitter

In an optical phased array, the emitters represent the final stage of the photonic circuit, where the guided optical signals are converted into radiated fields. The characteristics of these emitting elements play a central role in determining the angular distribution of the radiated beam and, therefore, the overall far-field response of the array.

As discussed in the previous section, the far-field pattern generated by an optical

phased array results from the combination of two contributions: the radiation pattern of the individual emitter and the interference between the fields emitted by the different channels of the array. The spatial distribution of the emitters, therefore, has a direct impact on the array factor and consequently on the angular characteristics of the radiated beam.

One of the most critical parameters in this context is the spacing between adjacent emitters, often referred to as the emitter pitch. Considering a linear array with uniform spacing d, the steering direction of the main beam is determined by the phase difference applied between the adjacent emitters. The constructive interference condition leads to

$$kd \sin \theta_0 + \Delta\phi = 0 \tag{5.6}$$

where $k = 2\pi/\lambda$ is the optical wavenumber, θ_0 is the beam direction, and $\Delta\phi$ is the phase shift between neighboring emitters.

The parameter d, often referred to as the *element spacing* or *emitter pitch*, represents the distance between adjacent radiating elements of the array. In integrated photonic implementations, the radiating elements correspond to the emitting waveguides located at the end of the photonic circuit. The pitch therefore corresponds to the center-to-center distance between adjacent waveguides.

The value of d strongly influences the angular characteristics of the far-field pattern. In particular, the pitch determines both the maximum steering angle that can be achieved and the possible appearance of secondary maxima in the radiation pattern.

From Eq. (5.6), the steering direction of the main beam can be expressed as

$$\sin \theta_0 = -\frac{\Delta\phi}{kd}, \tag{5.7}$$

where $\Delta\phi$ is the phase difference applied between adjacent emitters and $k = 2\pi/\lambda$ is the optical wavenumber. This expression shows that the steering angle depends directly on the emitter spacing: for a given phase gradient, increasing the pitch reduces the achievable angular steering range.

Another important consequence of the emitter spacing is the possible appearance of additional maxima in the far-field pattern. Two different types of secondary lobes can be distinguished. *Side lobes* are intrinsic features of finite arrays and originate from the interference between a limited number of emitters. Their presence depends mainly on the number of elements in the array and on the amplitude distribution across the emitters.

In contrast, *grating lobes* arise when the spacing between adjacent emitters becomes comparable to or larger than the optical wavelength. In this case multiple angular directions satisfy the constructive interference condition

$$kd(\sin \theta - \sin \theta_0) = 2\pi m \tag{5.8}$$

where m is an integer representing the order of the lobe. When this condition is satisfied for angles within the observable angular range, additional beams appear in the radiation pattern.

To avoid the appearance of grating lobes within the visible angular range, the emitter spacing must satisfy the condition

$$d \leq \frac{\lambda}{2}, \tag{5.9}$$

which corresponds to the spatial sampling criterion commonly adopted in phased array design [5]. When this requirement is satisfied, only a single main lobe appears in the radiation pattern and beam steering can be achieved without generating additional beams.

In integrated photonic implementations the emitter pitch is determined by the geometrical layout of the waveguides. Denoting the waveguide width as w and the gap between adjacent waveguides as g, the element spacing can be expressed as

$$d = w + g. \tag{5.10}$$

Reducing the gap g would therefore decrease the element spacing and increase the available steering range. However, excessively small gaps may introduce undesired optical coupling between neighboring waveguides, which can alter the intended phase distribution across the array.

To evaluate this effect, numerical simulations were performed to analyze the coupling between two adjacent waveguides as a function of their separation, and are reported in Fig. 5.2. The simulations were carried out using waveguides with a length of 500 µm and gap values of 1 µm, 2 µm and 3 µm. The optical signal was injected into the left waveguide in order to observe possible power transfer to the adjacent guide.

The results show that when the gap is reduced to 1 µm a strong coupling occurs almost immediately, leading to significant power transfer between the two waveguides. Increasing the separation to 2 µm significantly reduces this effect: only a very weak coupling can be observed near the end of the propagation length. For a gap of 3 µm no noticeable coupling is observed over the entire propagation distance.

These results indicate that both 2 µm and 3 µm gaps are suitable for the present design in terms of optical isolation between adjacent emitters. In the following sections both configurations will be considered in order to analyze how the resulting emitter pitch affects the far-field response of the array, in particular with respect to the presence of side lobes, the achievable steering angle and the overall radiation pattern.

In addition to the emitter spacing, the length of the emitting section also influences the characteristics of the radiated field. In integrate OPA implementations, the emitting waveguide acts as a distributed radiating aperture whose length affects both the radiation efficiency and the angular distribution of the emitted beam. In general, increasing the emitter length allows the optical field to radiate over a larger region, which improves the emission efficiency but also increases the overall footprint of the device. In contrast, very short emitters may limit the radiated power and broaden the radiation pattern. In the present design, a length of 100 µm was selected for the emitting waveguides as a compromise between efficient radiation and compact device dimensions.

Another important parameter affecting the far-field response is the number of emitters in the array. For a linear array composed of N elements, increasing the number of emitters effectively enlarges the aperture of the array, leading to a narrower main lobe in the far-field pattern and, therefore, to a higher angular resolution. For uniformly spaced emitters, the approximate angular width of the main lobe can be expressed as

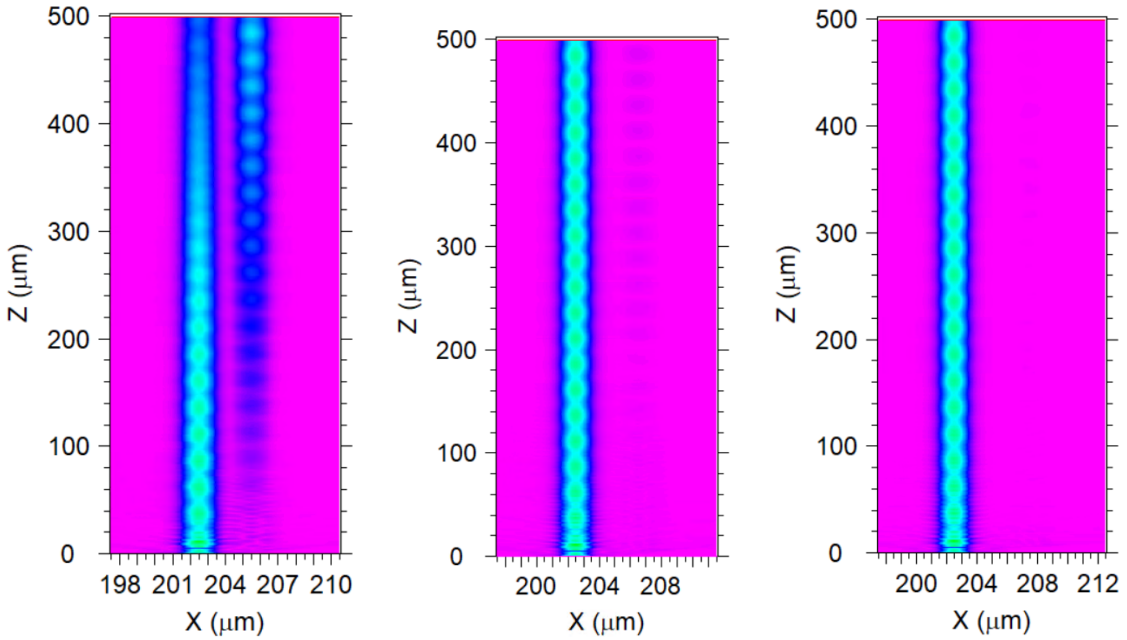

(a) $g = 1$ µm (b) $g = 2$ µm (c) $g = 3$ µm

Figure 5.2: Simulation of optical coupling between two adjacent waveguides for different gap values. The waveguides have a length of 500 µm and the optical signal is injected into the left waveguide. Strong coupling is observed for 1 µm spacing, while the coupling becomes negligible for 3 µm.

$$\Delta\theta \approx \frac{\lambda}{Nd} \tag{5.11}$$

where λ is the operating wavelength, N is the number of emitters, and d is the element spacing. This expression shows that the angular resolution improves as the number of emitters increases and as the spacing between them decreases.

In the present work, the array consists of $N = 16$ emitters operating at a wavelength of $\lambda = 6$ µm. Taking into account the two configurations introduced previously, corresponding to waveguide gaps of 2 µm and 3 µm, the resulting element spacing d determines the expected angular resolution of the array. According to Eq. 5.11, a smaller emitter spacing leads to a narrower main lobe and therefore to a higher angular resolution. The corresponding far-field patterns for the two geometrical configurations will be analyzed in the following sections, where the predicted behavior will be verified through numerical simulations of the complete array.

5.3 Calibration of Optical Phased Arrays

In an optical phased array, the far-field radiation pattern strongly depends on the relative phase of the optical signals emitted by the different channels of the array. Ideally, when

no beam steering is applied, all emitters should radiate with the same phase so that the fields interfere constructively along the normal direction, producing a collimated beam with a single main lobe.

In practice, however, this condition is rarely satisfied automatically. Because the optical signals propagate through different paths inside the photonic circuit, small differences in the optical path length inevitably arise between the various channels of the array. These differences introduce phase offsets between the emitters, resulting in a distorted far-field pattern characterized by multiple lobes and an irregular angular distribution. An example of this behavior is shown in Fig. 5.3, where the far-field pattern obtained before calibration exhibits several lobes resulting from the random phase relationship between the emitters.

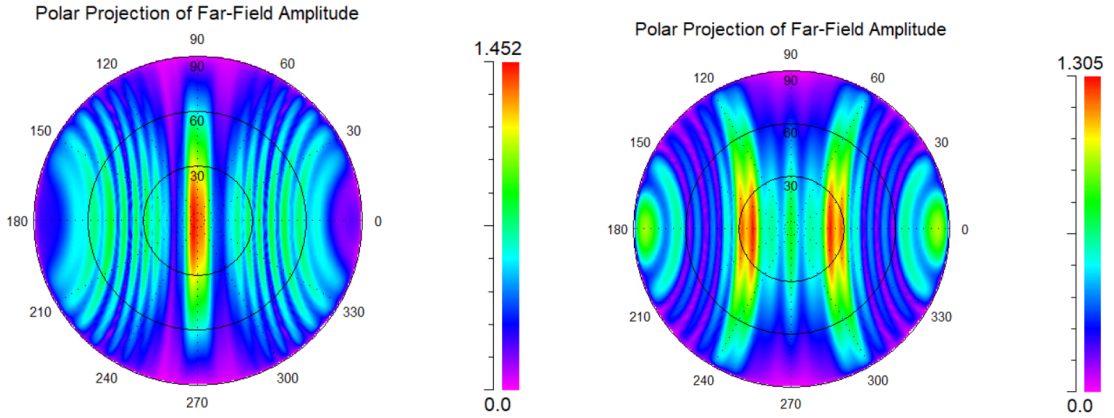

(a) Uncalibrated OPA with $d = 5\mu m$ (b) Uncalibrated OPA with $d = 4\mu m$

Figure 5.3: Far-field radiation patterns obtained before calibration for the two emitter spacings considered in this work. Because the optical paths of the emitters are different, the emitted fields exhibit random phase relationships, producing an irregular radiation pattern characterized by multiple lobes instead of a single collimated beam.

To obtain the desired radiation pattern, the phases of the emitters must be aligned so that the emitted fields interfere constructively in the desired direction. Ideally, this phase alignment should be achieved during the design stage by compensating for the different optical path lengths of the various channels.

The phase accumulated by an optical signal propagating along a waveguide is directly related to the optical path length. In particular, the phase shift introduced by a propagation length L can be expressed as

$$\phi = \beta L = \frac{2\pi}{\lambda} n_{\text{eff}} L \tag{5.12}$$

where β is the propagation constant, λ is the operating wavelength, and n_{eff} is the effective refractive index of the guided mode. From this relation it follows that a difference in the optical path length between two channels produces a corresponding phase difference

$$\Delta\phi = \frac{2\pi}{\lambda} n_{\text{eff}} \Delta L \tag{5.13}$$

This relation allows the phase mismatch between emitters to be compensated by properly adjusting their optical path length.

In the present work, the phase offset between the emitters was evaluated by placing optical monitors at the end of each emitter. The emitter exhibiting the largest phase value was used as a reference, and the optical paths of the remaining channels were adjusted in order to match this reference phase.

The compensation was achieved by introducing an additional straight waveguide section between the thermal phase-shifting region and the S-bend that connects the phase shifter to the emitter. By increasing the length of this intermediate waveguide segment, the optical path length of the corresponding channel can be precisely adjusted.

Since the emitter positions must remain fixed, the added straight segment is compensated by shortening the S-bend section that connects the phase shifter to the emitter. In this work, the S-bends are described by a raised-sine profile, whose geometry is given by

$$y(z) = \frac{H}{2}\left(1 - \cos\left(\frac{\pi z}{L}\right)\right) \tag{5.14}$$

where H is the vertical displacement and L is the length of the S-bend. Adjusting the straight segment therefore modifies the effective optical path while maintaining the fixed position of the emitters.

This approach allows the OPA to be partially calibrated already during the design stage, significantly reducing the phase mismatch between channels before any active tuning is applied. This is advantageous because, without such pre-compensation, the thermal phase shifters would need to correct large phase errors, leading to increased power consumption.

It should be noted that fabrication tolerances and process variations may still introduce residual phase errors that cannot be completely eliminated during the design stage. For this reason, active calibration using the phase shifters remains necessary. However, by compensating the main optical path differences during the design phase, the required phase correction becomes significantly smaller.

In practical implementations, this active calibration is typically performed using a feedback system capable of monitoring the far-field pattern and adjusting the phase shifters accordingly. An example of such a calibration technique is described in [6], where the phase errors are corrected iteratively using feedback from the measured optical output.

The effectiveness of the proposed pre-calibration method will be verified in the following section, where the far-field radiation pattern of the array will be analyzed. The expected result is a collimated beam with a dominant main lobe and strongly reduced phase-induced distortions, while residual side lobes may still appear due to the finite number of emitters and their spatial spacing.

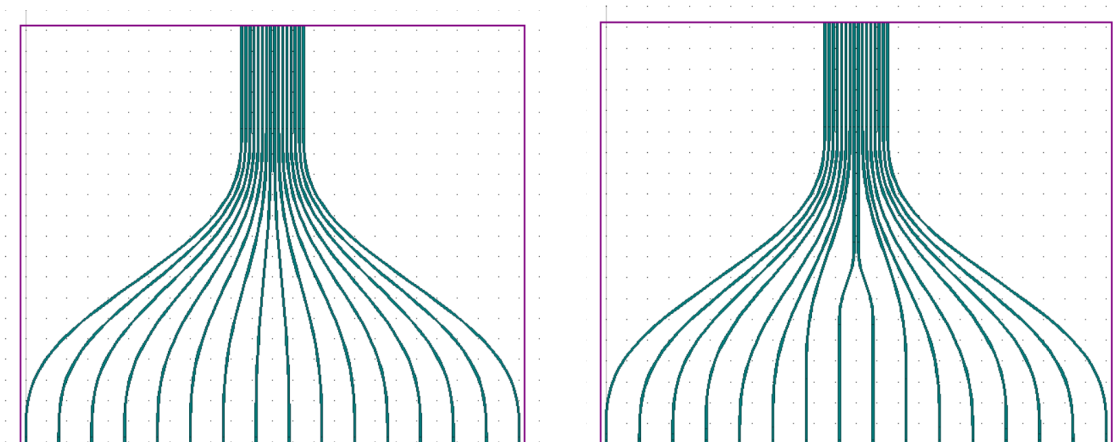

(a) Emitter region without optical path calibration.

(b) Emitter region after optical path calibration.

Figure 5.4: Conceptual representation of the optical path calibration procedure. By adjusting the optical path length between the phase shifter region and the emitters, the phase mismatch between channels can be reduced, enabling a more collimated far-field beam.

5.4 Far-Field Analysis of the Designed Optical Phased Array

The theoretical analysis presented in the previous sections allows an estimate of the radiation pattern expected from the designed optical phased array. When the emitters radiate with approximately equal phase, the emitted optical fields interfere constructively along a specific direction, producing a collimated beam characterized by a dominant main lobe. Because the array contains a finite number of emitters, secondary lobes may still appear in the radiation pattern. However, their amplitude is expected to be significantly lower than that of the main lobe.

Beam steering is obtained by introducing a progressive phase shift between adjacent emitters. The direction of the main lobe is related to the phase difference between neighboring emitters according to

$$\sin\theta_0 = -\frac{\Delta\phi}{kd} \tag{5.15}$$

where $\Delta\phi$ is the phase difference between adjacent emitters, $k = 2\pi/\lambda$ is the optical wavenumber, and d is the emitter spacing.

In practice, the maximum steering angle is limited by the maximum phase shift that can be introduced between adjacent emitters. In the present design, the maximum phase difference between two neighboring channels is limited to $\Delta\phi_{max} = 24°$. The maximum steering angle is therefore obtained when a linear phase gradient is applied across the entire array. In this condition, the phase shift between the two outermost emitters reaches 2π, while the phase shifts applied to the intermediate emitters are distributed linearly.

Using the maximum phase difference $\Delta\phi_{max} = 24°$ between adjacent emitters, the expected steering angle can be estimated from Eq. 5.15. For $\lambda = 6$ µm and $k = 2\pi/\lambda$, the theoretical maximum steering angles are approximately $\pm 4.6°$ for the configuration with $d = 5$ µm and $\pm 5.7°$ for $d = 4$ µm. These values provide a useful reference for interpreting the steering range observed in the far-field simulations.

The beamwidth of the main lobe can be estimated using the analytical expression reported in [3]

$$\Delta\phi_{FWHM} \approx \frac{0.886\,\lambda}{Nd\cos\phi} \tag{5.16}$$

where λ is the operating wavelength, N is the number of emitters, d is the emitter spacing, and ϕ is the steering angle. For the case of zero steering ($\phi = 0$) the relation simplifies to

$$\Delta\phi_{FWHM} \approx \frac{0.886\,\lambda}{Nd}. \tag{5.17}$$

Using $\lambda = 6$ µm and $N = 16$, the expected beamwidth is approximately $3.8°$ for $d = 5$ µm and $4.8°$ for $d = 4$ µm. These values provide a theoretical estimate that can be compared with the FWHM obtained from the far-field simulations.

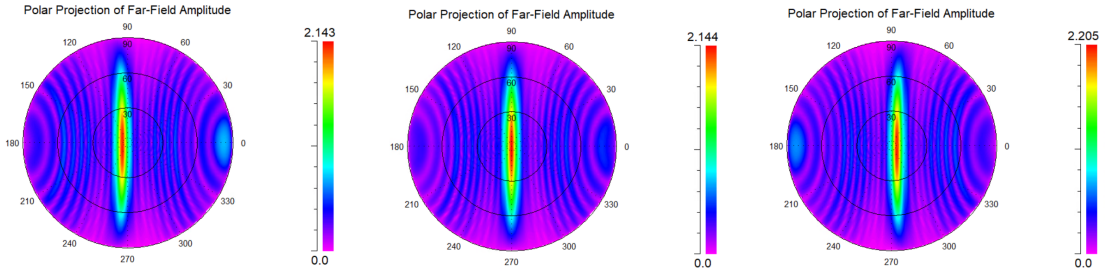

(a) Max steering (left) (b) Zero steering (c) Max steering (right)

Figure 5.5: Far-field radiation patterns obtained for the configuration with emitter spacing $d = 5$ µm.

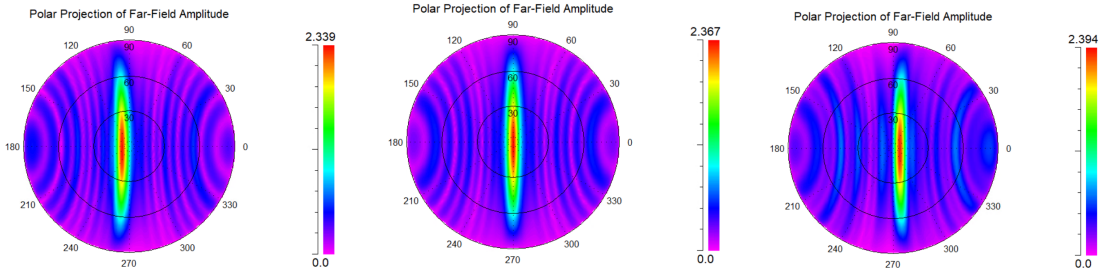

(a) Max steering (left) (b) Zero steering (c) Max steering (right)

Figure 5.6: Far-field radiation patterns obtained for the configuration with emitter spacing $d = 4$ µm.

The far-field radiation patterns obtained from the simulations are shown in Fig.s 5.5 and 5.6. For each configuration, three steering conditions are presented: maximum steering toward the left, zero steering, and maximum steering toward the right.

To quantitatively evaluate the radiation patterns, the steering angles and the full width at half maximum (FWHM) of the main lobe were extracted from the simulations, reported in Tab. 5.1

Emitter spacing (μm)	Steering angle (deg)	FWHM (deg)
$d = 5$	$[-4.6°,\ 4.6°]$	6.61
$d = 4$	$[-6°,\ 5.7°]$	7.43

Table 5.1: Steering angle and FWHM obtained from the far-field simulations.

The obtained results are consistent with the theoretical expectations. The configuration with the larger emitter spacing ($d = 5$ µm) produces a narrower main lobe compared to the $d = 4$ µm configuration. This behavior is consistent with the theoretical dependence of the beamwidth on the array aperture and emitter spacing.

Although the simulated FWHM values are higher than the analytical estimate, the observed trend agrees with the theoretical model. The difference can be attributed to the

radiation pattern of the individual emitters, the residual phase mismatches between the channels, and the finite size of the array.

Finally, it can be observed that the far-field patterns exhibit the presence of side lobes, whose amplitude is significantly lower than that of the main lobe. Compared with the uncalibrated case discussed in the previous section, the calibrated array produces a well-collimated beam with a clearly dominant main lobe, confirming the effectiveness of the proposed phase calibration strategy.

The complete architecture of the designed optical phased array is shown in Fig. 5.7. The first panel illustrates the layout of the device, including the cascaded MMI splitting network, the thermo-optic phase shifters, and the emitter array. The second panel shows the optical field propagation obtained from BeamPROP simulations at the design wavelength.

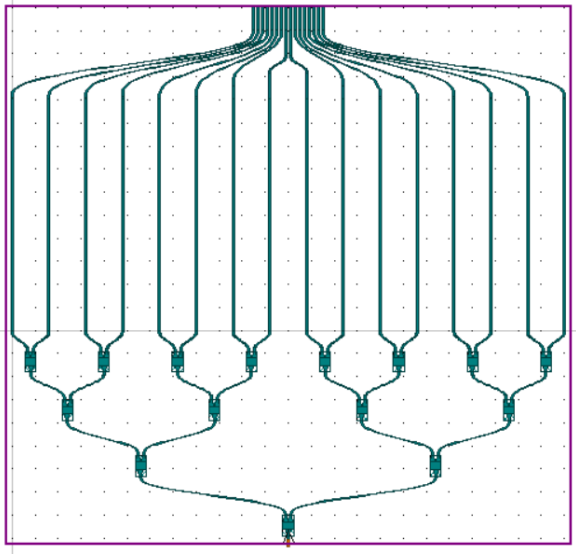

(a) Complete geometry of the optical phased array including the MMI splitting network, thermo-optic phase shifters, S-bend routing, and emitter array.

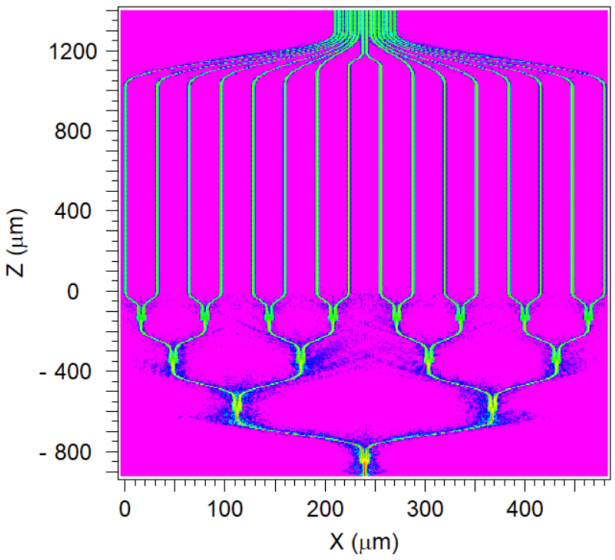

(b) Optical field propagation obtained from BeamPROP simulations at $\lambda = 6$ µm, showing the distribution of optical power from the input waveguide through the splitting network up to the emitter array.

Figure 5.7: Overview of the complete optical phased array structure used in this work. The first panel shows the geometrical layout of the device, while the second panel illustrates the simulated optical propagation along the circuit.

5.5 Imaging applications and random phase patterns

Optical phased arrays are commonly studied for beam steering applications, where a narrow optical beam is dynamically directed in different angular directions by applying controlled phase shifts between adjacent emitters. However, the ability to control the relative phases of multiple optical channels also enables a broader class of applications that go beyond simple beam steering. In particular, OPAs can be used to generate complex radiation patterns in the far field, which can be exploited in computational imaging systems.

In conventional optical imaging systems, information about a scene is typically acquired by scanning a focused beam across the field of view or by using detector arrays that directly capture the spatial distribution of light. These approaches often require complex optical systems or large arrays of detectors. Computational imaging techniques provide an alternative approach in which the scene is illuminated with a sequence of known optical patterns, and the image is reconstructed computationally from the measured signals. Among these approaches, single-pixel imaging has attracted significant attention in recent years. In this technique, the scene is illuminated by a sequence of spatially structured patterns, while a single detector measures the integrated optical response. The spatial information is then recovered through numerical reconstruction algorithms.

Optical phased arrays provide a particularly attractive platform for generating these structured illumination patterns in a compact and fully integrated device. By controlling the phase of the optical signals that feed the emitters, the interference of the radiated fields can be engineered to produce a wide variety of far-field distributions. When the phase difference between adjacent emitters follows a linear progression, the array generates a single collimated beam whose direction can be steered by adjusting the applied phase gradient. This regime is typically exploited in LiDAR and beam steering applications.

On the other hand, when arbitrary phase distributions are applied to the emitters, the resulting far-field pattern can become significantly more complex. Instead of a single main lobe, the radiation pattern may exhibit multiple lobes or speckle-like structures distributed across the angular range. These patterns can be interpreted as structured illumination profiles that can be used to encode spatial information about a scene.

Several recent works have explored the use of optical phased arrays for computational imaging applications. In particular, silicon photonic OPAs have been shown to allow for the generation of structured illumination patterns suitable for single-pixel imaging systems, where different phase configurations are applied to the emitters in order to produce a sequence of distinct far-field patterns [2].

An example of this concept is illustrated in Fig. 5.8, which shows the schematic of a single-pixel imaging system based on an optical phased array combined with a multimode fiber. In this configuration, the OPA generates a sequence of structured illumination patterns by applying different phase distributions to the emitters. These patterns are projected through the multimode fiber onto the target, while the transmitted or reflected optical signal is collected by a single detector.

If the k-th illumination pattern generated by the OPA is denoted by $I_k(x, y)$ and the object transmittance is $O(x, y)$, the measured signal can be written as

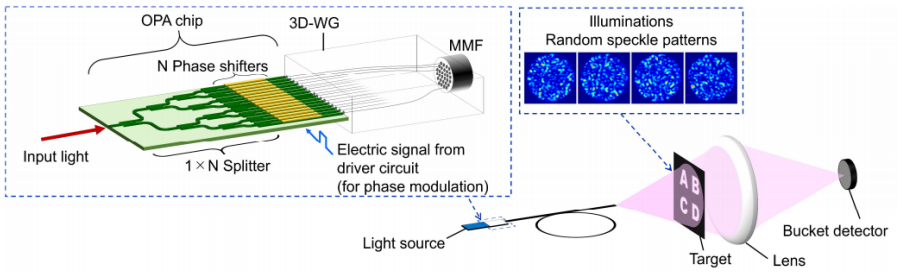

Figure 5.8: Schematic representation of a single-pixel imaging system based on a multimode fiber (MMF) and an optical phased array (OPA). The OPA generates a sequence of structured illumination patterns that are projected through the multimode fiber and used to reconstruct the image computationally. Reproduced from [2].

$$S_k = \iint I_k(x, y)\, O(x, y)\, dx\, dy. \tag{5.18}$$

By acquiring a sequence of measurements corresponding to different illumination patterns, the spatial information of the object can be reconstructed computationally.

A more detailed investigation of the generation and control of complex far-field patterns using optical phased arrays has been reported in [10]. In that work, the relationship between the phase configuration applied to the different branches of the array and the resulting radiation pattern is analyzed, showing that a wide variety of far-field profiles can be obtained by properly tuning the optical phases.

In particular, it is shown that while a linear phase progression leads to the generation of a single steered beam, arbitrary phase distributions can produce multi-lobe or speckle-like radiation patterns. These complex profiles can be exploited in applications where the goal is not only beam steering but also the generation of structured illumination patterns.

Furthermore, the study proposes a machine-learning assisted approach to determine the phase configuration required to reproduce a desired far-field distribution. By training a neural network with simulated far-field patterns, it becomes possible to predict the control phases needed to generate specific radiation profiles. This approach highlights the potential of combining integrated photonic devices with data-driven methods to simplify the control of complex optical systems.

Motivated by these considerations, additional simulations were performed on the optical phased array designed in this work in order to explore the radiation patterns obtained when random phase configurations are applied to the emitters. Starting from the calibrated configuration described in the previous section, random phase shifts were introduced in the different channels of the array. In this case, the constructive interference that produces a single collimated beam is intentionally disrupted, leading to far-field patterns characterized by multiple lobes distributed across the angular range.

Examples of these radiation patterns are shown in Fig. 5.9.

As expected, the resulting far-field distributions differ significantly from the single-lobe profiles observed in the calibrated beam steering regime. Instead, the radiation patterns exhibit irregular multi-lobe structures that resemble the structured illumination

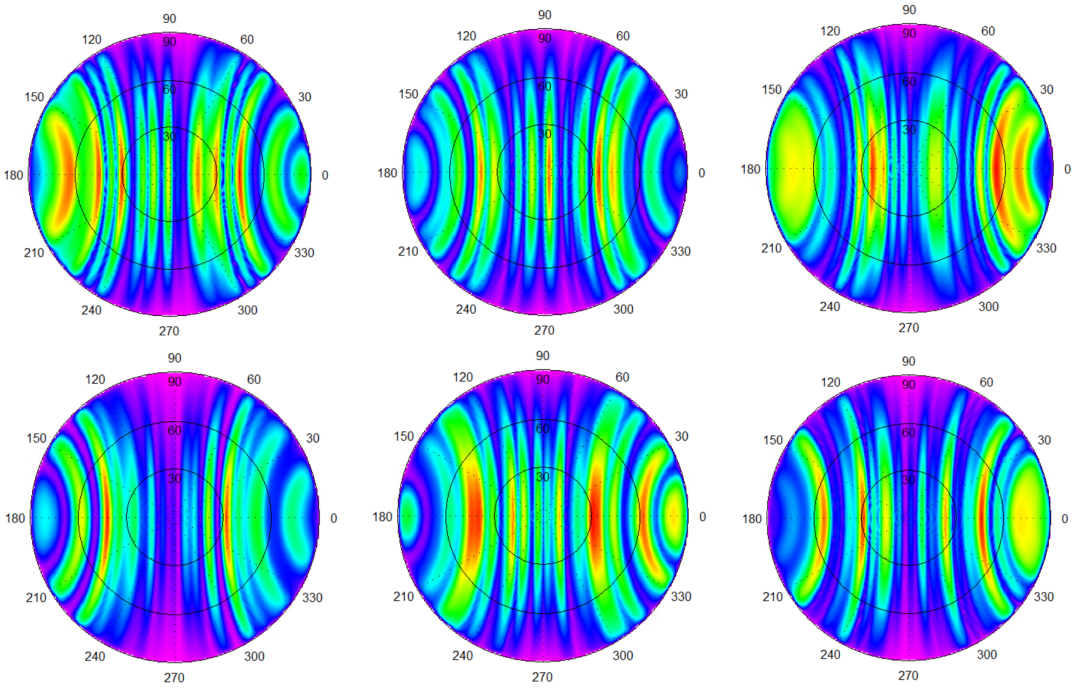

Figure 5.9: Examples of far-field radiation patterns obtained by applying random phase configurations to the emitters of the optical phased array. The resulting multi-lobe distributions resemble structured illumination patterns that can be exploited in computational imaging techniques.

patterns commonly employed in computational imaging approaches.

Although the optical phased array presented in this work has been primarily designed for beam steering applications in the mid-infrared range, these results illustrate how the same architecture could also be exploited in computational imaging systems. By dynamically varying the phase configuration applied to the emitters, the device could generate a sequence of illumination patterns suitable for imaging techniques based on structured illumination or compressed sensing.

Chapter 6

Conclusion

This work investigated the design of an integrated optical phased array operating in the mid-infrared spectral region on a germanium-on-silicon photonic platform. The goal of the study was to explore the feasibility of solid-state beam steering in the wavelength range between 4µm and 8µm, which is particularly relevant for sensing and LiDAR applications.

The analysis focused on the design and optimization of the main building blocks required for the realization of the device, including the waveguide platform, the optical power distribution network, the thermo-optic phase shifters, and the emitting array responsible for generating the far-field radiation pattern.

The work first addressed the definition of a suitable waveguide platform. A Ge-on-Si strip waveguide with air upper cladding was adopted as the basic guiding structure. Since the default material models available in the simulation tools do not accurately describe germanium absorption in the considered spectral range, a dedicated loss modeling procedure was implemented. Experimental values of waveguide attenuation reported in the literature were converted into equivalent complex refractive index values and incorporated into the simulation environment. This approach allowed the numerical model to reproduce realistic propagation losses across the entire wavelength range of interest. Based on this material model, the waveguide geometry was optimized by analyzing the effective indices of the first guided modes as a function of the waveguide width. A width of 2µm was selected as a suitable compromise between strong confinement of the fundamental mode and sufficient separation from higher-order modes. The routing of the optical signals within the circuit was also investigated through a comparison between circular bends and S-bend geometries. The raised-sine S-bend configuration was selected due to its lower propagation losses and greater flexibility in adapting the routing to the layout constraints of the device.

The second part of the work focused on the design of the power distribution network. Two possible architectures for the splitting stage were investigated, namely Y-splitters and multimode interference (MMI) couplers. After optimizing the geometrical parameters of both structures at the design wavelength of 6µm, their broadband performance was analyzed over the full operating range between 4µm and 8µm. The results showed that the MMI coupler exhibits significantly lower insertion losses and better power balance between the output ports across the considered wavelengths. For this reason, the final

architecture of the splitting network was implemented using cascaded 1×2 MMI couplers, allowing the optical power to be distributed to the sixteen emitters of the array.

The phase control stage was implemented using thermo-optic phase shifters integrated above the waveguides. The dependence of the effective refractive index on temperature was first analyzed in order to estimate the phase shift achievable for a given temperature variation. Based on this analysis, the length required to obtain a phase shift of 2π was determined, leading to a heater length of approximately 1 mm for the selected operating conditions. Thermal simulations were then performed using COMSOL to evaluate the temperature distribution generated by the heaters and to investigate the role of thermal isolation trenches. The simulations confirmed that the trenches significantly improve thermal confinement around the heated waveguide, reducing the required electrical power and limiting thermal cross-talk between adjacent channels.

The final part of the work addressed the design of the emitting array and the analysis of the far-field radiation pattern. The emitters were implemented as straight waveguide sections with a length of 100µm, arranged in a linear array. Particular attention was devoted to the selection of the emitter spacing, which directly influences both the beam steering range and the appearance of grating lobes. Coupling simulations between adjacent waveguides showed that a gap of 3µm effectively suppresses unwanted optical coupling, while smaller separations may introduce weak interactions over long propagation distances. Two configurations were therefore analyzed, corresponding to emitter pitches of 4µm and 5µm. A phase calibration procedure was implemented at the design stage to compensate for the phase differences arising from unequal optical path lengths within the circuit. This calibration allows the array to radiate with nearly uniform phase, producing a well-collimated beam in the far field.

The far-field simulations confirmed the expected behavior of the optical phased array. By applying a linear phase gradient across the emitters, the main beam can be steered within an angular range of approximately $\pm 4.6^\circ$ for the 5µm pitch configuration and about $\pm 6^\circ$ for the 4µm pitch configuration. The simulated radiation patterns exhibit a clearly dominant main lobe, with secondary lobes whose amplitude is significantly lower than that observed in the uncalibrated case. The measured beamwidths are consistent with the theoretical dependence of the full width at half maximum on the array aperture, confirming the validity of the adopted design approach.

Overall, the results demonstrate that the proposed architecture provides an effective solution for implementing integrated beam steering in the mid-infrared spectral region using a germanium-on-silicon photonic platform. The methodology developed in this work highlights the importance of combining realistic material modeling, careful geometrical optimization, and system-level considerations in the design of integrated OPAs. Although several practical aspects such as electrical routing, fabrication tolerances, and large-scale array integration were not explicitly addressed in this study, the presented results provide a solid basis for further development and experimental implementation of mid-infrared optical phased arrays.

Beyond beam steering applications, the results also highlight the versatility of optical phased arrays as programmable optical sources capable of generating complex radiation patterns. By applying different phase configurations to the emitters, the device can

produce structured far-field distributions that may be exploited in computational imaging systems based on structured illumination or single-pixel detection. This observation further extends the potential application space of the proposed architecture, suggesting possible future developments in integrated sensing and imaging systems.

Although the present study focused primarily on the design and numerical analysis of a 16-element OPA architecture, several aspects could be further investigated in future developments. In particular, the experimental validation of the proposed design, the optimization of the emitter radiation profile, and the extension of the architecture toward arrays with a larger number of emitters could further improve the achievable angular resolution of the system.

The results presented in this work therefore contribute to the understanding and design of integrated mid-infrared optical phased arrays and provide a useful foundation for the development of compact, solid-state beam steering systems based on germanium-on-silicon photonic platforms.

Bibliography

[1] CORNERSTONE. Germanium-on-silicon mpw design rules. Technical report, CORNERSTONE, 2024.

[2] Taichiro Fukui, Yusuke Kohno, Rui Tang, Yoshiaki Nakano, and Takuo Tanemura. Single-pixel imaging using multimode fiber and silicon photonic phased array. *Journal of Lightwave Technology*, 39(3):839–844, 2021.

[3] Yongjun Guo, Yuhao Guo, Chunshu Li, Hao Zhang, Xiaoyan Zhou, and Lin Zhang. Integrated optical phased arrays for beam forming and steering. *Applied Sciences*, 11(9), 2021.

[4] Jingwen He, Tao Dong, and Yue Xu. Review of photonic integrated optical phased arrays for space optical communication. *IEEE Access*, 8:188284–188298, 01 2020.

[5] Ilyas Abdinasir Kandid. *Array Design for High-Resolution Beam Steering in Optical Phased Arrays Applications*. PhD thesis, Carleton University, 2022.

[6] Li-Jing Li, Wen Chen, Xin-Yu Zhao, and Ming-Jie Sun. Fast optical phased array calibration technique for random phase modulation lidar. *IEEE Photonics Journal*, 11(1):1–10, 2019.

[7] D. Marris-Morini, Goran Mashanovich, Milos Nedeljkovic, Carlos Martins, Laurent Vivien, Jacopo Frigerio, and Giovanni Isella. Germanium-based mid-infrared photonics. *arXiv preprint*, May 2025.

[8] Milos Nedeljkovic, Jordi Soler Penades, Vinita Mittal, Ganapathy Senthil Murugan, Ali Khokhar, C. Littlejohns, Lewis Carpenter, Corin Gawith, James Wilkinson, and Goran Mashanovich. Germanium-on-silicon waveguides operating at mid-infrared wavelengths up to 8.5 um. *Optics Express*, 25:27431–27441, 10 2017.

[9] Mathias Prost, Yi-Chun Ling, Semih Cakmakyapan, Yu Zhang, Kaiqi Zhang, Junjie Hu, Yichi Zhang, and S. Yoo. Solid-state mwir beam steering using optical phased array on germanium-silicon photonic platform. *IEEE Photonics Journal*, PP:1–1, 11 2019.

[10] Daniele Savio and Paolo Bardella. Deep-learning assisted control of optical phased array: A case study. *IEEE Access*, 10:15421–15426, 2022.

[11] C. Xu et al. Simulation methodology for lidar-on-chip systems using optical phased arrays. *Optics Express*, 27(22):31600–31615, 2019.